

Population-level Task-evoked Functional Connectivity

Kun Meng^{1,*} and Ani Eloyan¹

¹Department of Biostatistics, Brown University School of Public Health, Providence, RI 02903, USA

*Corresponding Author, e-mail: kun_meng@brown.edu, Address: 121 S. Main St, Providence, RI 02903, USA.

March 2, 2021

Abstract

Functional magnetic resonance imaging (fMRI) is a non-invasive, in-vivo imaging technique essential for measuring brain activity. Functional connectivity is used to study associations between brain regions either at rest or while study participants perform tasks. This paper proposes a rigorous definition of task-evoked functional connectivity at the population level (ptFC). Importantly, our proposed ptFC is interpretable in the context of task-fMRI studies. Two algorithms for estimating ptFC are provided. We present the performance of the proposed algorithms compared to existing functional connectivity estimation approaches using simulations. Lastly, we apply the proposed framework to estimate functional connectivity in a motor-task study from the Human Connectome Project.

Keywords: AMUSE algorithm, Human Connectome Project, motor-task, weakly stationary with mean zero

1 Introduction

Functional magnetic resonance imaging (fMRI) is a non-invasive brain imaging technique used to estimate both brain regional activity and interactions between brain regions due to its ability to detect *neuronal activity* throughout the entire brain simultaneously. In a typical fMRI study, functional neuronal activity time courses are measured on three-dimensional volume elements (called *voxels*) during a certain period of time. Each time course is observed at discrete time points. For example, if the fMRI study lasts for 20 minutes and data are collected at every 2 seconds, i.e., the time between successive brain scans referred to

Abbreviations: BOLD, blood-oxygenation level-dependent; FC, functional connectivity; fMRI, functional magnetic resonance imaging; GLM, general linear models; HCP, Human Connectome Project; HRF, hemodynamic response function; iid, independent and identically distributed; ptFC, population-level task-evoked functional connectivity; ptFCE, population-level task-evoked functional connectivity estimation; ROI, region of interest; sd, standard deviation; TR, repetition time.

as *repetition time* (TR) is 2 seconds, then we obtain observations at 900 time points. In this paper, we are interested in investigating neuronal activity. However, since neuronal activity occurs in milliseconds, it is not possible to directly observe it using fMRI technology. It is implicitly captured by the *blood-oxygenation level-dependent* (BOLD) signals. Neuronal activity is followed by localized changes in metabolism. When the localized neuronal activity in a brain area occurs, the corresponding local oxygen consumption increases, and then oxygen-rich blood flows to this area. This process results in an increase in oxyhemoglobin and a decrease in deoxyhemoglobin. The BOLD signal value at each time point is the difference between the oxyhemoglobin and deoxyhemoglobin levels. The time course consisting of the BOLD signal values across all time points measures the localized metabolic activity influenced by the local vasculature of the brain, and it indirectly measures the localized neuronal activity. fMRI captures BOLD signals while the study participants are either resting (resting-state fMRI) or performing a task (task-fMRI).

We are interested in modeling brain neuronal activity and BOLD signals of participants ω , where $\omega \in \Omega$ and Ω is the collection of participants in the study. At each time point t , we denote by $Y_k(\omega; t)$ the BOLD signal value at the k^{th} node of participant ω 's brain. The word ‘‘node’’ throughout this paper refers to either a voxel or a *regions of interest* (ROI). Aggregated BOLD signals at a macro-area level are often of interest. That is, for each participant, BOLD signals are spatially averaged within pre-selected ROI and the resulting ROI-specific signals are analyzed. The BOLD signals for participant ω are represented by a K -vector-valued function $\{\mathbf{Y}(\omega; t) = (Y_1(\omega; t), Y_2(\omega; t), \dots, Y_K(\omega; t))^T \mid t \in \mathcal{T}\}$ on \mathcal{T} , where \mathcal{T} is the collection of time indices and K is the number of nodes. Furthermore, we assume that \mathcal{T} is a compact subset of \mathbb{R} . In this paper, we model three types of signals in the context of task-fMRI studies as illustrated in Figure 1: (i) the *stimulus signals* denoted by $N(t)$ representing the experimental design of the task of interest, (ii) the *task-evoked neuronal activity signals* at the k^{th} node $\Phi_k[\omega; N(t)]$ stemming from the task stimulus $N(t)$, where the ‘‘stimulus-to-activity’’ map $\Phi_k[\omega; \bullet] : N(t) \mapsto \Phi_k[\omega; N(t)]$ depends on participants ω , and (iii) the observed BOLD signals $Y_k(\omega; t) = \Psi_k\{\omega; \Phi_k[\omega; N(t)]\}$ that are associated with the task-evoked neuronal activity $\Phi_k[\omega; N(t)]$, where the ‘‘activity-to-BOLD’’ map $\Psi_k\{\omega; \bullet\} : \Phi_k[\omega; N(t)] \mapsto Y_k(\omega; t)$ is participant-dependent. In (ii) and (iii), the map $\Phi_k[\omega; \bullet]$ characterizes how neurons at the k^{th} node of ω react to stimulus $N(t)$, and the map $\Psi_k\{\omega; \bullet\}$ describes how neuronal activity $\Phi_k[\omega; N(t)]$ induces BOLD signal $Y_k(\omega; t)$. Therefore, we are interested in modeling signals $\Phi_k[\omega; N(t)]$. However, only BOLD signals $Y_k(\omega; t)$ are observable. The goal of many fMRI studies, including our proposed method, is to recover the information in $\Phi_k[\omega; \bullet]$ by analyzing $Y_k(\omega; t)$. In Section 2, we provide a nonparametric model for $\Phi_k[\omega; \bullet]$ and $\Psi_k\{\omega; \bullet\}$.

Theoretically, time t is a continuous variable and $\mathcal{T} = [0, t^*]$, where $0 < t^* < \infty$ denotes the end of the

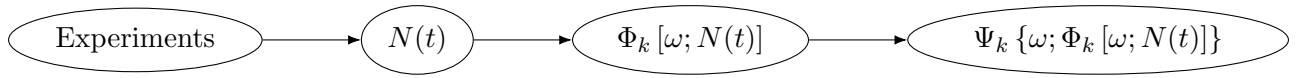


Figure 1: Stimulus signals $N(t)$ are known and determined by experimental designs of interest. For example, $N(t)$ are finite linear combinations of boxcar functions in block designs, and $N(t)$ are finite linear combinations of point masses in event-related designs. The task-evoked neuronal activity signals $\Phi_k[\omega; N(t)]$ responding to $N(t)$ are participant-dependent functions of $N(t)$, i.e., $\Phi_k[\omega; \bullet] : N(t) \mapsto \Phi_k[\omega; N(t)]$. Additionally, we assume $\Phi_k[\omega; N(t)] \equiv 0$ when $N(t) \equiv 0$, i.e., there is no task-evoked neuronal activity at the k^{th} node when there is no task stimulus. BOLD signals stem from $\Phi_k[\omega; N(t)]$ and are characterized by the participant-dependent maps $\Phi_k[\omega; N(t)] \mapsto \Psi_k\{\omega; \Phi_k[\omega; N(t)]\} = Y_k(\omega; t)$.

experiment. In applications, we obtain data only at discrete and finite time points in $\mathcal{T} = \{\tau \times TR | \tau = 0, 1, \dots, T\}$, where TR is the predetermined repetition time and T indicates that BOLD signals are observed at $T + 1$ time points. A BOLD signal, e.g., the one at the k^{th} node of participant ω , in task-fMRI consists of three components: (i) $P_k(\omega; t)$ denotes one evoked by the experimental task $N(t)$, (ii) $Q_k(\omega; t)$ denotes the one stemming from spontaneous brain activity and the neuronal activity responding to stimuli independent of $N(t)$, and (iii) the random error $\epsilon_k(\omega; t)$. Throughout this paper, we assume that these three components have an additive structure, and the observed BOLD signals $Y_k(\omega; t)$ are of the following form.

$$Y_k(\omega; t) = P_k(\omega; t) + Q_k(\omega; t) + \epsilon_k(\omega; t), \quad k = 1, 2, \dots, K, \quad (1.1)$$

where $P_k(\omega; t)$ are called *task-evoked terms*.

We implement the methods proposed in this paper to estimate functional connectivity in the context of understanding the human motor system. To investigate motor functional connectivity, we use a cohort of participants from a task-evoked functional MRI study publicly available at the Human Connectome Project (HCP, <https://protocols.humanconnectome.org/HCP/3T/task-fMRI-protocol-details.html>). The block-design motor task used in this study is adapted from experiments by Buckner et al. (2011) and Yeo et al. (2011), while details on the HCP implementation are given by Barch et al. (2013). During the experiment, the participants are asked to perform five different tasks when presented with a cue: tap their left/right fingers, squeeze their left/right toes, and move their tongues. BOLD signals $Y_k(\omega_j; t)$ are collected from 308 participants, i.e. the set of participants is defined as $\Omega = \{\omega_j\}_{j=1}^{308}$, while each BOLD signal is obtained with $TR = 0.72$ (seconds). Each experiment lasted for about 205 seconds, i.e., $T = 283$. We focus on the estimation of brain functional connectivity for the task of squeezing right toes. The stimulus signal has two 12-second task blocks, such that the onsets of these task blocks vary across participants ω_j . Nevertheless, the corresponding onsets of any two participants differ in less than 0.1 seconds. Therefore, we assume

that all participants share the same stimulus signal defined by $N(t) = N^{rt}(t) = \mathbf{1}_{[86.5,98.5)}(t) + \mathbf{1}_{[162,174)}(t)$.

In statistical analysis of task-fMRI data $\{\mathbf{Y}(\omega; t)\}_{t \in \mathcal{T}}$ defined by (1.1), two general topics are primarily of interest: (i) identification of nodes presenting task-evoked neuronal activity, i.e., the indices k such that $P_k(\omega; t) \neq 0$, and (ii) identification of task-evoked interactions between brain nodes. *General linear models* (GLM, Friston et al. (1994)) are commonly implemented to detect task-evoked nodes (Lindquist et al. (2008)). GLM is conducted at an individual node level and is not informative for investigating the interaction between nodes. Interactions between neuronal activity at pairs of nodes captured by BOLD signals are referred to as *functional connectivity* (FC) (Friston et al. (1993), Friston (1994), Friston et al. (1994), and Friston (2011)). FC observed during a task experiment tends to be different from that observed in a resting-state experiment (see Hampson et al. (2002) and Lowe et al. (2000)). The difference between task-fMRI and resting-state fMRI is presented by the non-zero task-evoked terms $P_k(\omega; t) \neq 0$. In this paper, we investigate the interactions between task-evoked terms $\{P_k(\omega; t)\}_{k=1}^K$. These interactions describe the FC structure stemming solely from the task stimulus $N(t)$ and reveal how information of $N(t)$ is transmitted across the brain. Specifically, rather than FC between BOLD signals $\{Y_k(\omega; t)\}_{k=1}^K$, we investigate the FC between task-evoked terms $\{P_k(\omega; t)\}_{k=1}^K$.

A considerable amount of work has been done to define and estimate FC between brain nodes. For example, Friston et al. (1993) defines FC as the temporal Pearson correlation between a pair of BOLD signals across time t . Following the Pearson correlation approach, one may measure the task-evoked FC between $P_k(\omega; t)$ and $P_l(\omega; t)$ by the absolute value of the Pearson correlation as follows

$$\left| \frac{\int_{\mathcal{T}} \left[P_k(\omega; t) - \frac{1}{\mu(\mathcal{T})} \int_{\mathcal{T}} P_k(\omega; s) \mu(ds) \right] \times \left[P_l(\omega; t) - \frac{1}{\mu(\mathcal{T})} \int_{\mathcal{T}} P_l(\omega; s) \mu(ds) \right] \mu(dt)}{\sqrt{\int_{\mathcal{T}} \left| P_k(\omega; t) - \frac{1}{\mu(\mathcal{T})} \int_{\mathcal{T}} P_k(\omega; s) \mu(ds) \right|^2 \mu(dt) \times \int_{\mathcal{T}} \left| P_l(\omega; t) - \frac{1}{\mu(\mathcal{T})} \int_{\mathcal{T}} P_l(\omega; s) \mu(ds) \right|^2 \mu(dt)}} \right|, \quad (1.2)$$

where, if $\mathcal{T} = [0, T^*]$, $\mu(dt)$ is the Lebesgue measure dt ; if $\mathcal{T} = \{\tau \times TR | \tau = 0, 1, \dots, T\}$, $\mu(dt)$ is the counting measure $\sum_{\tau \in \mathbb{Z}} \delta_{\tau \times TR}(dt)$, where $\delta_{\tau \times TR}$ is the point mass at time point $\tau \times TR$. There are many other approaches to defining and estimating FC developed in the last three decades. For example, *coherence analysis* (Müller et al. (2001), Sun et al. (2004)) is an analog of Pearson correlation in the Fourier frequency space and is a widely used method. Additionally, *beta-series regression* (Rissman et al. (2004)) is widely used as well for FC studies. These approaches have several limitations discussed in Section 2.2.

The paper is organized as follows. In Section 2, we propose a model for task-evoked BOLD signals; based on this model, we propose a rigorous and interpretable definition of task-evoked functional connectivity at

a population level (ptFC). In Section 3, we present two algorithms for estimating ptFC. We compare the performance of our proposed algorithms with existing approaches using simulations in Section 4. In Section 5, we apply the proposed approach to estimate the ptFC during a motor task using the publicly available HCP data set. Section 6 concludes the paper and provides further discussions.

2 Population-level Task-evoked Functional Connectivity (ptFC)

We first propose a model for BOLD signals at individual nodes. Using this model, we provide the definition of ptFC. Lastly, we list advantages of our proposed ptFC compared to existing approaches. To describe the statistical properties of the participant population Ω , we assume throughout this paper that an underlying probability space (Ω, \mathbb{P}) is defined on Ω , where \mathbb{P} is a probability measure (see Chapter 1.1 of Durrett (2019) for the definition of probability spaces and related materials).

2.1 Definition

Let $h_k(t)$ be the *hemodynamic response function* (HRF, Lindquist et al. (2008)) at the k^{th} node corresponding to the task stimulus $N(t)$ and shared by all participants $\omega \in \Omega$. For each participant ω , the GLM approach essentially models the task-evoked terms in (1.1) corresponding to $N(t)$ by

$$P_k(\omega; t) = \beta_k(\omega) \times (N * h_k)(t - t_{0,k}), \quad t \in \mathcal{T}, \quad \omega \in \Omega, \quad k = 1, 2, \dots, K. \quad (2.1)$$

where $\beta_k(\omega)$ is a GLM regression coefficient depending on ω , $t_{0,k}$ is a reaction delay time as the reaction of the k^{th} node to $N(t)$ at time t is not instantaneous, and the asterisk $*$ in $(N * h_k)$ denotes the convolution operation. Specifically, this is a GLM with response $\{P_k(\omega; t)\}_{t \in \mathcal{T}}$ and independent variable $\{(N * h_k)(t - t_{0,k})\}_{t \in \mathcal{T}}$, and the error term of this GLM is absorbed by the error $\{\epsilon_k(\omega; t)\}_{t \in \mathcal{T}}$ in (1.1). The task-evoked terms $P_k(\omega; t)$ in (2.1) contain the information of the neuronal activity evoked by the stimulus $N(t)$, and the quantity $\beta_k(\omega)$ measures the magnitude of the task-evoked neuronal activity. Visualizations of (2.1) are presented in Figure 2. Motivated by (1.1), we model the BOLD signals $Y_k(\omega; t)$ as follows.

$$Y_k(\omega; t) = \beta_k(\omega) \times (N * h_k)(t - t_{0,k}) + R_k(\omega; t), \quad t \in \mathcal{T}, \quad \omega \in \Omega, \quad k = 1, 2, \dots, K, \quad (2.2)$$

where the terms $R_k(\omega; t) = Q_k(\omega; t) + \epsilon_k(\omega; t)$, with $Q_k(\omega; t)$ and $\epsilon_k(\omega; t)$ defined in (1.1), are referred to as *reference terms* and contain the information of (i) the neuronal activity from stimuli independent of $N(t)$,

(ii) spontaneous neuronal activity, and (iii) random error. The model (2.2) is a random effects model and formally equivalent to the equation (1) in Warnick et al. (2018) and the equation (10) in Joel et al. (2011).

As described above, the task-evoked terms $P_k(\omega; t) = \beta_k(\omega) \times (N * h_k)(t - t_{0,k}) = \{[\beta_k(\omega) \times N(\cdot - t_{0,k})] * h_k\}(t)$ contain the information of the neuronal activity evoked by $N(t)$. In $P_k(\omega; t)$, HRF h_k represent metabolism and vasculature and do not characterize neuronal activity. Therefore, we model neuronal activity signals $\Phi_k[\omega; N(t)]$ responding to $N(t)$ (see Figure 1) as $\beta_k(\omega) \times N(t - t_{0,k})$. Using model (2.2), the “stimulus-to-activity” map $\Phi_k[\omega; \bullet]$ and the “activity-to-BOLD” map $\Psi_k\{\omega; \bullet\}$ in Figure 1 are expressed as follows.

$$\begin{aligned} \Phi_k[\omega; \bullet] &: N(t) \mapsto \beta_k(\omega) \times N(t - t_{0,k}), \\ \Psi_k\{\omega; \bullet\} &: \Phi_k[\omega; N(t)] = \beta_k(\omega) \times N(t - t_{0,k}) \mapsto \{\Phi_k[\omega; N(\cdot)] * h_k\}(t) + R_k(\omega; t) = Y_k(\omega; t). \end{aligned} \quad (2.3)$$

The reference terms $R_k(t)$ in (2.2) are general. Here, we provide an explicit example of $R_k(t)$ suitable for most applications. Let $\tilde{N}_\gamma(t)$, for $\gamma = 1, 2, \dots, \Gamma$, define the stimulus signals other than the experimental task of interest $N(t)$. Let $\tilde{h}_{k,\gamma}(t)$ be the HRF at the k^{th} node corresponding to stimulus $\tilde{N}_\gamma(t)$, for $\gamma = 1, 2, \dots, \Gamma$. Then the explicit example of $R_k(t)$, for $k = 1, 2, \dots, K$, is presented as follows.

$$R_k(\omega; t) = Q_k(\omega; t) + \epsilon_k(\omega; t), \text{ where } Q_k(\omega; t) = \left\{ \sum_{\gamma=1}^{\Gamma} \tilde{\beta}_{k,\gamma}(\omega) \times \left(\tilde{N}_\gamma * \tilde{h}_{k,\gamma} \right) (t - t_{0,k,\gamma}) \right\} + S_k(\omega; t), \quad (2.4)$$

where $t_{0,k,\gamma}$ is the reaction delay of the k^{th} node corresponding to stimulus $\tilde{N}_\gamma(t)$, $\tilde{\beta}_\gamma(\omega)$ depends on participants ω , $S_k(\omega; t)$ is the BOLD signal component arising from spontaneous neuronal activity at the k^{th} node of ω , and $\epsilon_k(\omega; t)$ is the random noise at the k^{th} node of participant ω . In the HCP motor task study, $\Gamma = 4$ stimuli other than $N^{rt}(t)$ of interest are tapping left and right fingers, squeezing left toes, and moving the tongue. These four stimuli are independent of $N^{rt}(t)$ and are not of interest when estimating the FC evoked by the task of interest; applying the notations in (2.4) to this example, stimulus signals of these four stimuli are represented as $\tilde{N}_1(t) = \mathbf{1}_{[71.35,83.35]}(t) + \mathbf{1}_{[177.125,189.125]}(t)$, $\tilde{N}_2(t) = \mathbf{1}_{[11,23]}(t) + \mathbf{1}_{[116.63,128.63]}(t)$, $\tilde{N}_3(t) = \mathbf{1}_{[26.13,38.13]}(t) + \mathbf{1}_{[146.88,158.88]}(t)$, and $\tilde{N}_4(t) = \mathbf{1}_{[56.26,68.26]}(t) + \mathbf{1}_{[131.75,143.75]}(t)$.

FC is expected to characterize the mechanism of neuronal activity rather than metabolism or vasculature. Therefore, the task-evoked FC is defined using the task-evoked neuronal activity signals $\Phi_k[\omega; N(t)]$. In model (2.3) of $\Phi_k[\omega; N(t)]$, stimulus signals $N(t)$ are fully determined by experimental design. Additionally, the reaction delay $t_{0,k}$ affects HRF h_k since the task-evoked terms can be expressed as $P_k(\omega; t) = \{[\beta_k(\omega) \times N] * [h_k(\cdot - t_{0,k})]\}(t)$. Therefore, the task-evoked FC is expected to be determined by coefficients $\beta_k(\omega)$.

Since $\beta_k(\omega)$, for $k = 1, 2, \dots, K$, measure the magnitude of the neuronal activity evoked by task stimulus $N(t)$, the k^{th} and l^{th} nodes are functionally connected at the population level during the task if one of the following scenarios holds: (i) for participants with strong reaction to $N(t)$ at the k^{th} node, their l^{th} nodes' reaction to $N(t)$ is strong as well and vice versa, i.e., they are positively correlated; (ii) for participants with strong reaction to $N(t)$ at the k^{th} nodes, their l^{th} nodes' reaction to $N(t)$ is weak and vice versa, i.e., they are negatively correlated. Furthermore, we make the following two modeling assumptions on the distribution of $\beta_k(\omega)$ across all participants $\omega \in \Omega$: (1) If there exists a connection evoked by task $N(t)$ between k^{th} and l^{th} nodes, the corresponding random coefficients $\beta_k(\omega)$ and $\beta_l(\omega)$ are approximately linearly associated. (2) Each variance $\mathbb{V}\beta_k = \mathbb{E}(\beta_k^2) - (\mathbb{E}\beta_k)^2$, for $k = 1, 2, \dots, K$, is strictly positive, i.e., random variable $\beta_k : \omega \rightarrow \beta_k(\omega)$ is not deterministic[†]; this assumption is realistic as it allows the variability of task-evoked neuronal activity $\beta_k(\omega) \times N(t - t_{0,k})$ across population Ω . Since the correlation $\text{corr}(\beta_k, \beta_l) = \frac{\mathbb{E}(\beta_k\beta_l) - (\mathbb{E}\beta_k)(\mathbb{E}\beta_l)}{\sqrt{\mathbb{V}\beta_k} \times \sqrt{\mathbb{V}\beta_l}}$ measures the linear statistical correlation between β_k and β_l , we define ptFC as follows.

Definition 2.1. For each ω in a population of interest Ω , the BOLD signal $Y_k(\omega; t)$ at the k^{th} node, for $k = 1, 2, \dots, K$, is of the form (2.2). Then the ptFC between the k^{th} and l^{th} nodes is defined as $|\text{corr}(\beta_k, \beta_l)|$.

An advantage of Definition 2.1 is its scale-invariance. Since task-evoked term $\beta_k(\omega) \times (N * h_k)$ can be represented as $\frac{\beta_k(\omega)}{c_1 \times c_2} \times [(c_2 N) * (c_1 h_k)]$, the scale of $\beta_k(\omega)$ changes if we change the scale of HRF h_k or $N(t)$ in our model. However, $\text{corr}(\beta_k, \beta_l)$ is invariant to scaling transforms $\beta_{k'} \mapsto c\beta_{k'}$, for $k' \in \{k, l\}$, so is ptFC $|\text{corr}(\beta_k, \beta_l)|$. This scale-invariance solves the potential issue of identifiability and interpretability of β_k .

2.2 Advantages

In this subsection, we present advantages of our proposed ptFC in Definition 2.1 compared to existing approaches. We first discuss the limitations of the Pearson correlation approach (1.2) using model (2.1). Plugging (2.1) into (1.2), we obtain the following measurement of association between $P_k(\omega; t)$ and $P_l(\omega; t)$.

$$|\text{corr}(P_k, P_l)| := \left| \frac{\int_{\mathcal{T}} \left[\phi_k(t) - \frac{1}{\mu(\mathcal{T})} \int_{\mathcal{T}} \phi_k(s) \mu(ds) \right] \times \left[\phi_l(t) - \frac{1}{\mu(\mathcal{T})} \int_{\mathcal{T}} \phi_l(s) \mu(ds) \right] \mu(dt)}{\sqrt{\int_{\mathcal{T}} \left| \phi_k(t) - \frac{1}{\mu(\mathcal{T})} \int_{\mathcal{T}} \phi_k(s) \mu(ds) \right|^2 \mu(dt)} \times \sqrt{\int_{\mathcal{T}} \left| \phi_l(t) - \frac{1}{\mu(\mathcal{T})} \int_{\mathcal{T}} \phi_l(s) \mu(ds) \right|^2 \mu(dt)}} \right|, \quad (2.5)$$

where $\phi_{k'}(t) = N * h_{k'}(t - t_{0,k'})$ for $k' \in \{k, l\}$, and (2.5) reveals the following limitations of Pearson correlation approach (1.2).

[†] Expectation \mathbb{E} is associated with probability measure \mathbb{P} . Specifically, $\mathbb{E}(\beta_k^\nu) = \int_{\Omega} \beta_k(\omega)^\nu \mathbb{P}(d\omega)$, for all $\nu \in \mathbb{N}$.

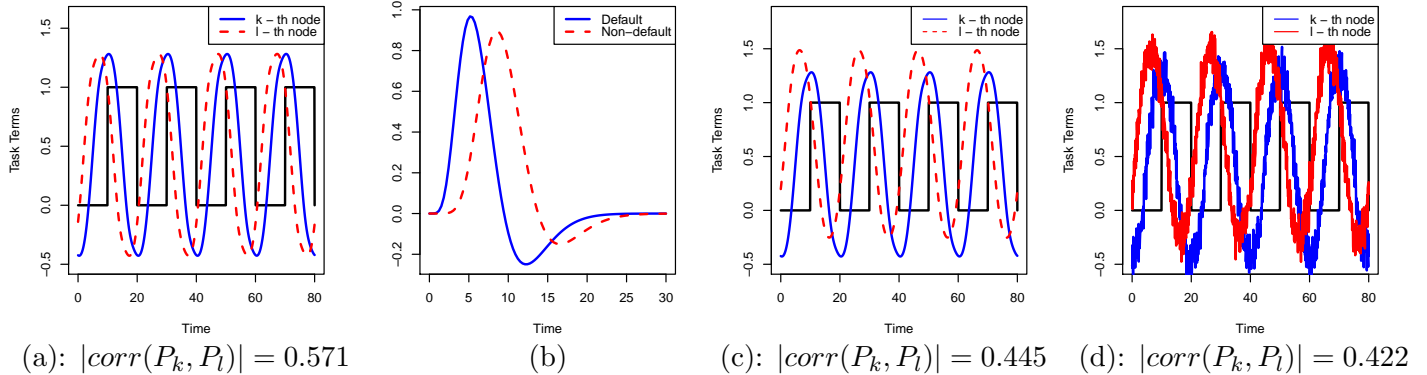


Figure 2: An example illustrating the limitations of (2.5). Let $N(t) = \sum_{m=1}^4 \mathbf{1}_{(20m-10, 20m]}(t)$ be the stimulus signal of a block design, $\mathcal{T} = [0, 80]$, and h_k be the `canonicalHRF` function with default parameters in the R package `neuRosim`. h_k is illustrated by the blue curve in (b). Panel (a) shows the influence of the variation in reaction delay on (2.5), where $h_l(t) = h_k(t + 3)$, i.e., $t_{0,k} = -3$; the task-evoked terms at the k^{th} and l^{th} nodes are presented by blue and red curves, respectively. In (b), h_l is replaced by the `canonicalHRF` function with parameters $\mathbf{a1} = 10, \mathbf{a2} = 15, \mathbf{b1} = \mathbf{b2} = 0.9, \mathbf{c} = 0.35$, and presented by the red (dashed) curve. Panel (c) shows the influence of variation in HRF on (2.5), and the task-evoked terms at the k^{th} and l^{th} nodes are presented by blue and red curves, respectively, where h_l is defined in (b) as the red curve. Panel (d) is a noise-contaminated version of (c), i.e., curves of $P_k(t) + \epsilon_k(t)$ (blue) and $P_l(t) + \epsilon_l(t)$ (red) with $\epsilon_k(t), \epsilon_l(t) \sim_{iid} N(0, 0.1)$ for each t . Panel (d) shows that random noise can further influence (2.5). In panels (a,c,d), the presented $|corr(P_k, P_l)|$ is defined in (1.2).

Only nuisance parameters: Based on the reasoning in Section 2.1, the information on the mechanism of the task-evoked neuronal activity is contained in coefficients $\beta_k(\omega)$. Hence, it is counterintuitive that (2.5) does not depend on $\beta_k(\omega)$ and depends only on the nuisance parameters $N(t)$ and h_k when considering quantification of brain neuronal activity. For example, if the k^{th} node does not react to $N(t)$, then the task-evoked term $\beta_k(\omega) \times (N * h_k)(t - t_{0,k})$ is expected to be approximately zero, i.e., $\beta_k(\omega) \approx 0$, and there should be no task-evoked interaction between k^{th} and all other nodes. However, (2.5) can still be very large as the non-reaction information contained in $\beta_k(\omega) \approx 0$ vanishes. In contrast with (2.5), the ptFC in Definition 2.1 is based on $\{(\beta_k(\omega), \beta_l(\omega)) | \omega \in \Omega\}$, rather than nuisance parameters.

Variation in reaction delay: Reaction delay times $t_{0,k}$ may vary across nodes (for example, see Miezin et al. (2000) for the investigation of the left and right visual and motor cortices and the corresponding difference between response onsets). If $t_{0,k} \neq t_{0,l}$, for example $t_{0,k} < t_{0,l}$, then it is likely that the k^{th} node reacts to the task-stimulus $N(t)$ first, and then the neuronal activity at the k^{th} node causes that at the l^{th} node. Because of this potential causality represented by the difference between $t_{0,k}$ and $t_{0,l}$, it is natural to expect that the k^{th} and l^{th} nodes are likely functionally connected. However, the measurement (2.5) can be very small if $t_{0,k} \neq t_{0,l}$ and may not reveal the true interaction between neuronal activity of two nodes. An

example of this issue is illustrated in Figure 2 (a). Since our proposed definition of ptFC does not involve reaction delay times, the variation in reaction delay does not influence the ptFC in Definition 2.1.

Variation in HRF: HRF can heavily vary across brain nodes (Buckner et al. (1998), Lee et al. (2001), Miezin et al. (2000), Saad et al. (2001), Schacter et al. (1997), Rosen et al. (1998)). Since task-evoked FC is not expected to depend on HRF, variation of HRF in different brain regions should not influence task-evoked FC. However, the quantity defined in (2.5) can be small if $h_k \neq h_l$ as illustrated by the example in Figure 2 (c). Given that our proposed definition of ptFC does not involve the information of HRF, it is invariant to the variation in HRF across brain nodes.

The beta-series regression approach is widely accepted. However, its estimation procedure is based on GLM and involves modeling HRF across all nodes. Since the HRF may vary across nodes, node-wise HRF modeling is cumbersome, and the inaccuracy in modeling reduces the efficacy of beta-series regression. Our proposed approach for defining ptFC and the forthcoming algorithms for estimating ptFC do not involve modeling HRF and hence are not influenced by node dependent variability in HRF.

Coherence analysis based estimation of task-evoked FC is not influenced by any of the issues discussed above. In this approach, FC between BOLD signals $Y_k(\omega; t)$ and $Y_l(\omega; t)$ is measured by the *coherence* evaluating the extent of the *linear time-invariant relationship* between these two signals via Fourier frequencies. The linear time-invariant relationship is equivalent to that there exists a (generalized) function κ such that $Y_k(t) = \kappa * Y_l(t)$ or $Y_l(t) = \kappa * Y_k(t)$ (Theorem 1.2 of Hörmander (1960)), implying that the corresponding coherence is equal to 1 at all frequencies. However, there is no guarantee that the relationship between two BOLD signals is linear time-invariant if the corresponding two nodes are functionally connected. Additionally, the mathematical formulation implemented in Müller et al. (2001) and Sun et al. (2004) has limited interpretability. Equation (2) in Müller et al. (2001) and equation (3) in Sun et al. (2004) apply the autocovariance defined as the expected value $\mathbb{E}[Y_k(\tau + t)Y_l(t)]$. However, the underlying probability space and distribution for conducting the expectation \mathbb{E} operation is not clearly interpreted therein. In the proposed definition of ptFC, we clearly specify the underlying probability space for expectation \mathbb{E} .

3 Estimation Algorithms

In this section, we propose two algorithms to estimate ptFC. Our proposed estimation algorithms do not depend on any parametric assumptions and are based on Fourier transforms. Since BOLD signals in applications are observed only at discrete and finite time points, in the sequel, we set the collection of time indices \mathcal{T} to be $\{\tau \times TR | \tau = 0, 1, \dots, T\}$ and $t = \tau \times TR$ for some index $\tau \in \{0, 1, \dots, T\}$. Before introducing the

estimation algorithms, we provide notations for (discrete) Fourier transforms. Further materials on Fourier transforms can be found in Bloomfield (2004). For any function $f : \mathcal{T} \rightarrow \mathbb{R}$, we extend f as follows to be a periodic function on $\{\tau' \times TR | \tau' \in \mathbb{Z}\}$

$$f(\tau' \times TR) = f(\tau \times TR), \quad \tau' \equiv \tau \pmod{T+1} \text{ for } \tau = 0, 1, \dots, T \text{ and all } \tau' \in \mathbb{Z}. \quad (3.1)$$

In this paper, all functions defined on \mathcal{T} are automatically extended using (3.1) to be periodic functions on $\{\tau' \times TR | \tau' \in \mathbb{Z}\}$. The (discrete) convolution $(N * h_k)(t)$ is defined by $(N * h_k)(\tau \times TR) = \frac{1}{T+1} \sum_{\tau'=0}^T N(\tau' \times TR) h_k((\tau - \tau') \times TR)$ for all $t = \tau \times TR$ with $\tau = 0, 1, \dots, T$. We define the Fourier transform of f as

$$\widehat{f}(\xi) := \frac{1}{T+1} \sum_{\tau=0}^T f(\tau \times TR) e^{-2\pi i \xi (\tau \times TR)} \text{ for all } \xi \in \mathbb{R}. \quad (3.2)$$

It is straightforward that $\widehat{f}(\xi)$ is a periodic function with period $1/TR$.

Additionally, a technical assumption for our proposed algorithms is $\mathbb{E}\beta_k = \mathbb{E}R_k(t) = 0$, for $k = 1, 2, \dots, K$ and $t \in \mathcal{T}$ motivated by the following centralization.[†]

$$Y_k(\omega; t) - \mathbb{E}Y_k(t) = [\beta_k(\omega) - \mathbb{E}\beta_k] (N * h_k)(t - t_{0,k}) + [R_k(\omega; t) - \mathbb{E}R_k(t)]. \quad (3.3)$$

Using $[\beta_k(\omega) - \mathbb{E}\beta_k]$ as $\beta_k(\omega)$ and $[R_k(\omega; t) - \mathbb{E}R_k(t)]$ as $R_k(\omega; t)$, we model the demeaned outcome. If the reference terms $R_k(\omega; t)$ satisfy (2.4), centralization (3.3) allows us to assume $\mathbb{E}\tilde{\beta}_{k,\gamma} = \mathbb{E}S_k(t) = \mathbb{E}\epsilon_k(t) = 0$ for all $k = 1, 2, \dots, K, \gamma = 1, 2, \dots, \Gamma$, and $t \in \mathcal{T}$.

3.1 ptFC Estimation (ptFCE) Algorithm

In this subsection, we propose the ptFCE algorithm for the estimation of ptFC in studies where both task-evoked signals $Y_k(\omega; t)$ and reference signals $R_k(\omega; t)$ are observed. In the next subsection, we propose an algorithm based on ptFCE applicable in experiments where only task-evoked signals $Y_k(\omega; t)$ are available.

In Section 2.1, our proposed definition of ptFC, given by $|\text{corr}(\beta_k, \beta_l)|$, does not depend on reaction delay times $t_{0,k}$ or reference terms $R_k(\omega; t)$. To construct an estimator of $|\text{corr}(\beta_k, \beta_l)|$ using the observed BOLD signals, we note that applying the periodic extension (3.1) to function $(N * h_k)$, it is easy to verify that the two stochastic processes $(N * h_k)(t - t_{0,k} - U(\omega))$ and $(N * h_k)(t - U(\omega))$, where the random variable $U : \Omega \rightarrow \mathcal{T}, \omega \mapsto U(\omega)$ is uniformly distributed on \mathcal{T} , are identically distributed. In the meantime,

[†] Throughout this paper, for any real-valued stochastic process $\{Z(\omega; t) | \omega \in \Omega\}_{t \in \mathcal{T}}$, the expected value $\mathbb{E}Z(t)$ denotes the average of $Z(\omega; t)$ across all $\omega \in \Omega$, i.e., $\int_{\Omega} Z(\omega; t) \mathbb{P}(d\omega)$, for each fixed $t \in \mathcal{T}$.

$(N * h_k)(t - U(\omega))$, and hence the distribution of $(N * h_k)(t - t_{0,k} - U(\omega))$, does not depend on the nuisance parameter $t_{0,k}$. Therefore, we investigate the following time-shifted signals

$$Y_k(\omega; t - U(\omega)) = \beta_k(\omega)(N * h_k)(t - t_{0,k} - U(\omega)) + R_k(\omega; t - U(\omega)), \text{ for } k = 1, 2, \dots, K, \quad (3.4)$$

Based on the discussion above, the distributions of $Y_k(\omega; t - U(\omega))$ do not depend on the nuisance parameter $t_{0,k}$. Then, we consider the autocovariance $\mathbb{E}[Y_k(t - U)Y_l(t + s - U)]$ when estimating the ptFC between nodes k and l , where $s = \underline{s} \times TR$ with indices $\underline{s} \in \mathbb{Z}$. Additionally, ptFC $|corr(\beta_k, \beta_l)|$ only depends on task-evoked terms $[Y_k(\omega; t - U(\omega)) - R_k(\omega; t - U(\omega))]$ (see (3.4)). Hence, we investigate the autocovariance differences $\mathbb{E}[Y_k(t - U)Y_l(t + s - U)] - \mathbb{E}[R_k(t - U)R_l(t + s - U)]$ obtained by filtering out the reference terms from the observed BOLD signals. If $U(\omega)$, $\{\beta_k(\omega)\}_{k=1}^K$, and $\{R_k(\omega; t)|t \in \mathcal{T}\}_{k=1}^K$ are independent, Theorem 8.1 in the Appendix implies that this autocovariance difference depends only on s and does not depend on t . Then we denote this difference of interest as follows.

$$\mathcal{A}_{kl}(s) = \mathbb{E}[Y_k(t - U)Y_l(t + s - U)] - \mathbb{E}[R_k(t - U)R_l(t + s - U)], \quad s = \underline{s} \times TR \text{ for all } \underline{s} \in \mathbb{Z}, \quad (3.5)$$

for $k, l = 1, 2, \dots, K$. Finally, we propose the following estimator for ptFC $|corr(\beta_k, \beta_l)|$ by incorporating a normalization multiplier in (3.5).

$$\mathcal{C}_{kl}(\xi) := \frac{|\widehat{\mathcal{A}}_{kl}(\xi)|}{\sqrt{|\widehat{\mathcal{A}}_{kk}(\xi)| |\widehat{\mathcal{A}}_{ll}(\xi)|}}, \quad \text{for all } \xi \in \mathbb{R}, \quad (3.6)$$

where $\widehat{\mathcal{A}}_{kl}(\xi)$ denotes the Fourier transform of $\mathcal{A}_{kl}(s)$ defined in (3.2). Periodicity property of the Fourier transform implies that $\mathcal{C}_{kl}(\xi)$ is a periodic function of ξ with period $1/TR$. Lemma 8.1 in the Appendix implies that the ratio in (3.6) is well-defined for all $\xi \in [0, 1/TR]$ except for at most finitely many points ξ such that $\widehat{\mathcal{A}}_{kk}(\xi)\widehat{\mathcal{A}}_{ll}(\xi) = 0$. Importantly, based on Theorem 8.1, we obtain $\mathcal{C}_{kl}(\xi) = |corr(\beta_k, \beta_l)|$, for all $\xi \in \mathbb{R}$, i.e., $\mathcal{C}_{kl}(\xi)$ is an unbiased estimator of ptFC for all ξ under the model (2.2). An algorithm for computing $\mathcal{C}_{kl}(\xi)$ in (3.6) will be provided in this subsection. In the implementation of the algorithm, the random variable $U(\omega)$ is artificially generated and automatically independent of $\{\beta_k(\omega), R_k(\omega; t)|t \in \mathcal{T}, k = 1, 2, \dots, K\}$.

The model for BOLD signals (2.2) is based on the assumption that the reference terms $R_k(\omega; t) = Q_k(\omega; t) + \epsilon_k(\omega; t)$ contain the total random noise $\epsilon_k(\omega; t)$. However, in applications it is more realistic to assume that the reference terms contain only a part of the random noise $\epsilon_k(\omega; t)$. Specifically, we assume that

the random noise $\epsilon_k(\omega; t)$ can be additively decomposed into two parts $\epsilon_k(\omega; t) = V_k(\omega; t) + W_k(\omega; t)$, where the reference terms can be used to model only a part of the random noise, i.e., $R_k(\omega; t) = Q_k(\omega; t) + V_k(\omega; t)$, and $W_k(\omega; t) = W_k(\omega; t)$ is the “residual noise” not modeled by $R_k(\omega; t)$. Therefore, it is more realistic to model task-evoked BOLD signals $Y_k(t)$ by the following “noise-contaminated” version of (2.2).

$$Y_k(\omega; t) := \beta_k(\omega) \times N * h_k(t - t_{0,k}) + W_k(\omega; t) + R_k(\omega; t), \quad t \in \mathcal{T}, \quad \omega \in \Omega, \quad k = 1, 2, \dots, K. \quad (3.7)$$

Before modeling residual noise $W_k(\omega; t)$, we introduce a concept: a vector-valued stochastic process $\{G(\omega; t) = (G_1(\omega; t), G_2(\omega; t), \dots, G_K(\omega; t))^T\}_{t \in \mathcal{T}}$ is called *weakly stationary with mean zero* if $\mathbb{E}G_k(t) = 0$, for all $t \in \mathcal{T}$, and $\mathbb{E}[G_k(t)G_l(t+s)]$ depends only on s , rather than t , for all k, l . We assume $\{W(\omega; t) := (W_1(\omega; t), W_2(\omega; t), \dots, W_K(\omega; t))^T\}_{t \in \mathcal{T}}$ satisfies (i) $W(\omega; t_1)$ is independent of $W(\omega; t_2)$ if $t_1 \neq t_2$, (ii) $\Sigma_{kl} = \mathbb{E}[W_k(t)W_l(t)]$ for all $t \in \mathcal{T}$, and (iii) $W(\omega; t)$ is weakly stationary with mean zero. If $\{W(\omega; t)\}_{t \in \mathcal{T}}$, $U(\omega)$, $\{\beta_k(\omega)\}_{k=1}^K$, and $\{R_k(\omega; t)|t \in \mathcal{T}\}_{k=1}^K$ are independent, Theorem 8.2 in the Appendix implies

$$\mathcal{C}_{kl}(\xi) = \frac{\left| \mathbb{E}(\beta_k \beta_l) \frac{\widehat{h}_k(\xi) \widehat{h}_l(\xi)}{|\widehat{h}_k(\xi) \widehat{h}_l(\xi)|} e^{2\pi i \xi(t_{0,k} - t_{0,l})} + \frac{\Sigma_{kl}}{(T+1)|\widehat{N}(\xi)|^2 |\widehat{h}_k(\xi) \widehat{h}_l(\xi)|} \right|}{\sqrt{\left(\mathbb{E}(\beta_k^2) + \frac{\Sigma_{kk}}{(T+1)|\widehat{N}(\xi) \widehat{h}_k(\xi)|^2} \right) \left(\mathbb{E}(\beta_l^2) + \frac{\Sigma_{ll}}{(T+1)|\widehat{N}(\xi) \widehat{h}_l(\xi)|^2} \right)}}, \quad \text{for all } \xi \in \mathbb{R}, \quad (3.8)$$

where $\mathcal{C}_{kl}(\xi)$ is defined in (3.6). For a fixed T , (3.8) implies $\mathcal{C}_{kl}(\xi) \approx |\text{corr}(\beta_k, \beta_l)|$ at frequencies ξ such that $|\widehat{h}_k(\xi)|$ and $|\widehat{h}_l(\xi)|$ are sufficiently large. For most models of HRF h_k , the absolute value of Fourier transform $|\widehat{h}_k(\xi)|$ takes large values when $\xi \in (0, 0.1)$, e.g., the examples in Figure 3. Therefore, we estimate the ptFC $|\text{corr}(\beta_k, \beta_l)|$ by the median of $\mathcal{C}_{kl}(\xi)$ across $\xi \in (0, 0.1)$. Based on the estimator $\mathcal{C}_{kl}(\xi)$ in (3.6) and the discussion above on the choice of ξ , we propose the *population-level task-evoked functional connectivity estimation (ptFCE) algorithm* (Algorithm 1) for the estimation of ptFC.

To calculate the $\mathcal{C}_{kl}(\xi)$, we need to estimate two components using data from the experiment of interest. The component $\mathbb{E}[Y_k(t-U)Y_l(t+s-U)]$ is estimated using the task-evoked BOLD signals $Y_k(\omega; t)$, and $\mathbb{E}[R_k(t-U)R_l(t+s-U)]$ is estimated using the reference terms $R_k(\omega; t)$. Therefore, the experiment may be designed as follows: during the first half of the experiment, a resting-state scan is obtained and reference signals $R_k(\omega; t)$ are collected; in the second half, the scans stimulus $N(t)$ is implemented, and task-evoked BOLD signals $Y_k(\omega; t)$ are collected. However, not all experiments are designed to include a resting-state segment. If the reference terms $R_k(\omega; t)$ are not available, a compromised approach proposed in the next subsection may be used for estimation.

Algorithm 1 ptFCE Algorithm:

Input: (i) Task-evoked signals $\{\mathbf{Y}(\omega_j; \tau \times TR) = (Y_k(\omega_j; \tau \times TR), Y_l(\omega_j; \tau \times TR))\}_{\tau=0}^T$ of participants $\{\omega_j\}_{j=1}^M$ in population Ω ; (ii) reference signals $\{\mathbf{R}(\omega_j; \tau \times TR) = (R_k(\omega_j; \tau \times TR), R_l(\omega_j; \tau \times TR))\}_{\tau=0}^T$ of participants $\{\omega_j\}_{j=1}^M$; (iii) repetition time TR .

Output: An estimation of the ptFC $|corr(\beta_k, \beta_l)|$ between the k^{th} and l^{th} nodes.

1: **Zero-mean:** For each $\tau = 0, 1, \dots, T$ and $j = 1, 2, \dots, M$, do

$$\begin{aligned}\mathbf{Y}(\omega_j; \tau \times TR) &\leftarrow \mathbf{Y}(\omega_j; \tau \times TR) - \frac{1}{M} \sum_{j'=1}^M \mathbf{Y}(\omega_{j'}; \tau \times TR), \\ \mathbf{R}(\omega_j; \tau \times TR) &\leftarrow \mathbf{R}(\omega_j; \tau \times TR) - \frac{1}{M} \sum_{j'=1}^M \mathbf{R}(\omega_{j'}; \tau \times TR).\end{aligned}$$

- 2: For each $j = 1, 2, \dots, M$, periodically extend $\mathbf{Y}(\omega_j, \tau \times TR)$ and $\mathbf{R}(\omega_j, \tau \times TR)$ using (3.1).
3: Generate M integers $\{u_j\}_{j=1}^M$ from the uniform distribution on $\{0, 1, 2, \dots, T\}$.
4: For each $\underline{s} = 0, 1, 2, \dots, T$ and $(k', l') \in \{(k, l), (k, k), (l, l)\}$, compute

$$\begin{aligned}\mathcal{A}_{k'l'}(\underline{s} \times TR) &\leftarrow \frac{1}{T+1} \sum_{\tau=0}^T \{\mathcal{E}_y(\tau; \underline{s}) - \mathcal{E}_r(\tau; \underline{s})\}, \quad \text{where} \\ \mathcal{E}_y(\tau; \underline{s}) &\leftarrow \frac{1}{M} \sum_{j=1}^M \left\{ Y_{k'}(\omega_j; (\tau - u_j) \times TR) \times Y_{l'}(\omega_j; (t + \underline{s} - u_j) \times TR) \right\}, \\ \mathcal{E}_r(\tau; \underline{s}) &\leftarrow \frac{1}{M} \sum_{j=1}^M \left\{ R_{k'}(\omega_j; (\tau - u_j) \times TR) \times R_{l'}(\omega_j; (t + \underline{s} - u_j) \times TR) \right\}.\end{aligned}$$

- 5: For all $\xi \in (0, 1/(2 \times TR))$, compute the Fourier transforms $\widehat{\mathcal{A}}_{kl}(\xi)$, $\widehat{\mathcal{A}}_{kk}(\xi)$, and $\widehat{\mathcal{A}}_{ll}(\xi)$ using (3.2).
6: Compute $\mathcal{C}_{kl}(\xi) \leftarrow |\widehat{\mathcal{A}}_{kl}(\xi)| / (|\widehat{\mathcal{A}}_{kk}(\xi)\widehat{\mathcal{A}}_{ll}(\xi)|)^{1/2}$.
7: Estimate the ptFC $|corr(\beta_k, \beta_l)|$ by the median of $\mathcal{C}_{kl}(\xi)$ across all $\xi \in (0, 0.1)$.
-

3.2 AMUSE-ptFCE Algorithm

In many applications, the reference signals $R_k(\omega; t)$ are not available. To estimate ptFC when reference signals are not available, we apply the *AMUSE algorithm* (Tong et al. (1991)) to estimate reference signals and then ptFC are estimated using the ptFCE algorithm provided in Section 3.1. As a result, we propose the AMUSE-ptFCE algorithm (Algorithm 2).

First, we note that $\mathbb{E}[(N * h_k)(t - t_{0,k} - U)]$ is a deterministic constant not depending on t , and we denote this constant by C_k . Define the stochastic processes $J_k(\omega; t) = \beta_k(\omega) [(N * h_k)(t - t_{0,k} - U(\omega)) - C_k]$, for $k = 1, 2, \dots, K$. For each fixed k , using (8.1) in the Appendix, one can verify that the scalar-valued stochastic process $J_k(\omega; t)$ is weakly stationary with mean zero conditioning on β_k , then $\mathbb{E}\{J_k(t) \times J_k(t + s) | \beta_k\}$ depends only on s . The following theorem gives the foundation for the AMUSE-ptFC algorithm.

Theorem 3.1. For each fixed $k \in \{1, 2, \dots, K\}$, suppose task-evoked BOLD signals $Y_k(\omega; t)$, for $\omega \in$

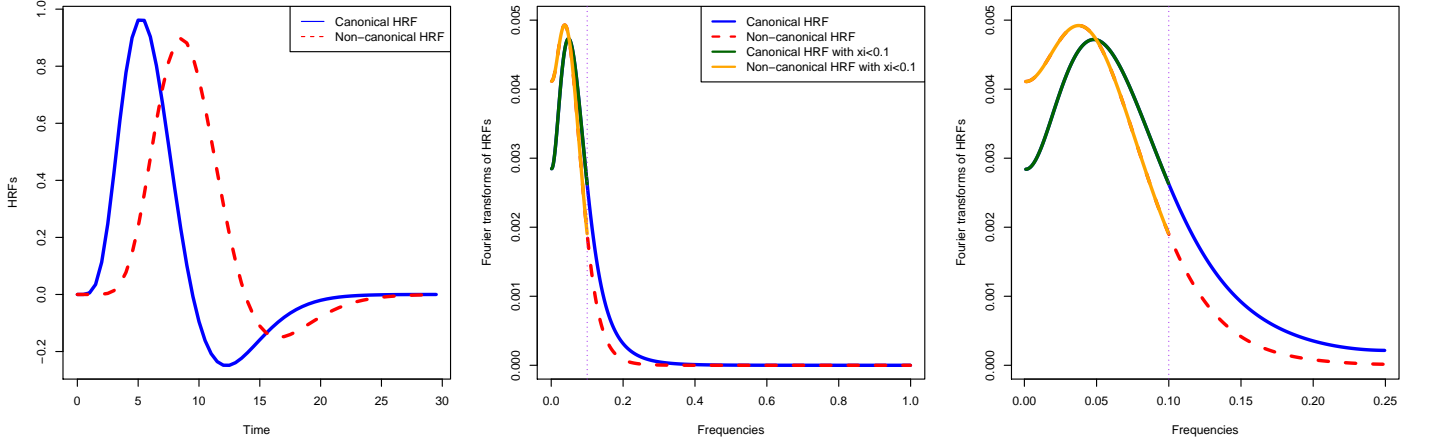


Figure 3: The canonical HRF (blue solid curve in the left panel) is plotted using the `canonicalHRF` function in the R package `neuRosim` with default parameters. An example non-canonical HRF (red dashed curve in the left panel) is constructed by changing the function parameters to $\mathbf{a1}=10$, $\mathbf{a2}=15$, $\mathbf{b1}=\mathbf{b2}=0.9$, $\mathbf{c}=0.35$. The middle panel shows the absolute values of the Fourier transforms of these two HRF when $TR = 0.5$. The right panel shows the absolute values of the Fourier transforms of these two HRF when $TR = 2$. In both the middle and right panels, we plot the curves only in the corresponding semiperiod intervals $(0, 1/(2TR))$.

Ω , are of the form in (2.2), the scalar-valued stochastic process $\{R_k(\omega; t)\}_{t \in \mathcal{T}}$ is weakly stationary with mean zero, and the random variable $U : \Omega \rightarrow \mathcal{T}$ is uniformly distributed. Additionally, for each fixed k , $\beta_k(\omega)$, $\{R_k(\omega; t)\}_{t \in \mathcal{T}}$, and $U(\omega)$ are independent, and there exists $t_k^* \in \mathcal{T}$ such that $\frac{\mathbb{E}\{J_k(t)J_k(t-t_k^*)|\beta_k\}}{\mathbb{E}\{J_k(t)^2|\beta_k\}} \neq \frac{\mathbb{E}\{R_k(t)R_k(t-t_k^*)\}}{\mathbb{E}\{R_k(t)^2\}}$. If the matrix $\mathbf{A} = (a_{ij})_{1 \leq i, j \leq 2}$ and the stochastic process $\{\mathbf{s}(\omega; t) = (s_1(\omega; t), s_2(\omega; t))^T\}_{t \in \mathcal{T}}$ satisfy (i) given β_k , $\mathbf{s}(\omega; t)$ is weakly stationary with mean zero, (ii) $\mathbb{E}[s_1(t)s_2(t+s)|\beta_k] = 0$ for all t and s , (iii) $\frac{\mathbb{E}\{s_1(t)s_1(t-t_k^*)|\beta_k\}}{\mathbb{E}\{s_1(t)|\beta_k\}} \neq \frac{\mathbb{E}\{s_2(t)s_2(t-t_k^*)|\beta_k\}}{\mathbb{E}\{s_2(t)|\beta_k\}}$, and

$$\mathbf{A} \begin{pmatrix} s_1(\omega; t) \\ s_2(\omega; t) \end{pmatrix} = \begin{pmatrix} 1 & 1 \\ \frac{1}{\beta_k(\omega)} & 0 \end{pmatrix} \begin{pmatrix} J_k(\omega; t) \\ R_k(\omega; t - U(\omega)) \end{pmatrix} = \begin{pmatrix} Y_k(\omega; t - U(\omega)) - \beta_k(\omega)C_k \\ (N * h_k)(t - t_{0,k} - U(\omega)) - C_k \end{pmatrix}, \quad (3.9)$$

for all $t \in \mathcal{T}$, then there exist a diagonal matrix $\mathbf{\Lambda}$ and a permutation matrix \mathbf{P} , such that

$$\begin{pmatrix} 1 & 1 \\ \frac{1}{\beta_k(\omega)} & 0 \end{pmatrix} = \mathbf{A}\mathbf{\Lambda}^{-1}\mathbf{P}^{-1} \text{ and } \begin{pmatrix} J_k(\omega; t) \\ R_k(\omega; t - U(\omega)) \end{pmatrix} = \mathbf{P}\mathbf{\Lambda}\mathbf{s}(\omega; t), \text{ for all } t \in \mathcal{T}. \quad (3.10)$$

The proof of Theorem 3.1 is provided in the Appendix. For each k and ω , the pair $(\mathbf{A}, \mathbf{s}(\omega; t))$ in (3.9) can be derived by the AMUSE algorithm with the following 2-vector-valued signal as its input.

$$\left\{ (Y_k(\omega; t - U(\omega)) - \beta_k(\omega)C_k, (N * h_k)(t - t_{0,k} - U(\omega)) - C_k)^T \mid t \in \mathcal{T} \right\}. \quad (3.11)$$

In our proposed AMUSE-ptFCE algorithm, we assume that $h_k(t)$ and $t_{0,k}$ are known. For example, we may set $t_{0,k} = 0$ and $h_k(t)$ to be the R function `canonicalHRF` with default parameters. Since $h_k(t)$, $t_{0,k}$, $N(t)$, and the distribution of $U(\omega)$ are known, the constants C_k are known. However, the coefficients $\beta_k(\omega)$ are unknown, and then the input (3.11) is not available in applications. Since $\mathbb{E}\beta_k = 0$, in applications, we ignore the term $\beta_k(\omega)C_k$ in (3.11) and apply

$$\left\{ (Y_k(\omega; t - U(\omega)), (N * h_k)(t - t_{0,k} - U(\omega)) - C_k)^T \mid t \in \mathcal{T} \right\}$$

as the input of the AMUSE algorithm for deriving $(\mathbf{A}, \mathbf{s}(\omega; t))$ instead of (3.11). To approximately recover reference terms $R_k(\omega; t)$ from the pair $(\mathbf{A}, \mathbf{s}(\omega; t))$ in (3.9), we show the following result.

Theorem 3.2. *For each $k \in \{1, 2, \dots, K\}$ and $\omega \in \Omega$, suppose the pair $(\mathbf{A}, \mathbf{s}(\omega; t))$ satisfies (3.10). Then there exists $i' \in \{1, 2\}$ such that $a_{1i'}s_{i'}(\omega; t) = J_k(\omega; t)$.*

The proof of Theorem 3.2 is in the Appendix. In applications, the index i' in Theorem 3.2 is computed as $i' = \operatorname{argmax}_i \{ \operatorname{corr}(s_i(\omega; t), (N * h_k)(t - t_{0,k} - U(\omega_j)) - C_k) \}$, across $t \mid i = 1, 2$. The AMUSE algorithm and Theorem 3.2 approximately recover $J_k(\omega; t) = \beta_k(\omega)(N * h_k)(t - t_{0,k} - U(\omega)) - \beta_k(\omega)C_k$. Again, we ignore the term $\beta_k(\omega)C_k$ as $\mathbb{E}\beta_k = 0$, i.e., $J_k(\omega; t) \approx \beta_k(\omega)(N * h_k)(\omega; t - t_{0,k} - U(\omega))$. Then we obtain

$$R_k(\omega; t) \approx Y_k(\omega; t) - J_k(\omega; t), \text{ for all } k = 1, 2, \dots, K \text{ and } \omega \in \Omega. \quad (3.12)$$

Given the estimated reference terms in (3.12), we may apply Algorithm 1 to estimate ptFC. The estimation procedure provided above is summarized in the AMUSE-ptFC algorithm (Algorithm 2) for the estimation of ptFC in cases where reference terms are not available.

Although the AMUSE-ptFCE algorithm is based only on the task-evoked signals and omits $\beta_k(\omega)C_k$ terms, its performance is comparable with that of ptFCE algorithm, which applies both task-evoked and reference signals, if random noise is large as illustrated in Section 4. While it may seem counterintuitive that large noise helps improve the estimation accuracy of AMUSE-ptFCE, a possible explanation of this phenomenon is that estimation bias from omitting $\beta_k(\omega)C_k$ is overwhelmed by large random noise. The R code for performing estimation using the ptFCE and AMUSE-ptFCE algorithms is available at <https://github.com/KMengBrown/Population-level-Task-evoked-Functional-Connectivity.git>.

Algorithm 2 AMUSE-ptFCE Algorithm

Input: (i) Task-evoked signals $\{\mathbf{Y}(\omega_j; \tau \times TR) = (Y_k(\omega_j; \tau \times TR), Y_l(\omega_j; \tau \times TR))^T\}_{\tau=0}^T$ of participants $\{\omega_j\}_{j=1}^M$ in population Ω ; (ii) repetition time TR ;
(iii) the stimulus signal $\{N(\tau \times TR)\}_{\tau=0}^T$ corresponding to the task of interest;
(iv) reaction delay times $t_{0,k'} = \tau_{0,k'} \times TR$ with some $\tau_{0,k'} \in \mathbb{Z}$ for $k' \in \{k, l\}$, and their default values are $t_{0,k'} = 0$ for $k' \in \{k, l\}$;
(v) HRF $h_{k'}$ for $k' \in \{k, l\}$, and the default HRF are $h_k = h_l =$ the R function `canonicalHRF` with its default parameters.

Output: An estimation of the ptFC $|corr(\beta_k, \beta_l)|$ between the k^{th} and l^{th} nodes.

- 1: Generate M integers $\{u_j\}_{j=1}^M$ from the uniform distribution on $\{1, 2, \dots, T\}$.
- 2: **for** $k' \in \{k, l\}$ **do**,
- 3: Compute $C_{k'} \leftarrow \frac{1}{M} \sum_{j=1}^M N * h_{k'}((\tau - \tau_{0,k'} - u_j) \times TR)$.
- 4: **for** $j = 1, 2, \dots, M$ **do**
- 5: Apply the AMUSE Algorithm using the following 2-dimensional signal as an input

$$\left\{ (Y_{k'}(\omega_j; (\tau - u_j) \times TR), N * h_{k'}((\tau - \tau_{0,k'} - u_j) \times TR) - C_{k'})^T \mid \tau = 0, 1, \dots, T \right\}.$$

The AMUSE algorithm returns a 2-dimensional signal $\{(s_1(\tau \times TR), s_2(\tau \times TR))^T \mid \tau = 0, 1, \dots, T\}$ and an unmixing matrix \mathbf{Q} . Let $\mathbf{M} = (m_{\mu\nu})_{1 \leq \mu, \nu \leq 2}$ be the (Moore-Penrose generalized) inverse of \mathbf{Q} .

- 6: **for** $i = 1, 2$ **do**
 - 7: Compute the Pearson correlation between $\{s_i(\tau \times TR)\}_{\tau=0}^T$ and $\{(N * h_{k'})((\tau - \tau_{0,k'} - u_j) \times TR) - C_{k'}\}_{\tau=0}^T$ and denote the absolute value of this correlation as r_i .
 - 8: **end for**
 - 9: Compute $i^* = \operatorname{argmax}_i \{r_i \mid i = 1, 2\}$.
 - 10: Update $Y_{k'}(\omega_j; \tau \times TR) \leftarrow m_{1i^*} \times s_{i^*}(\tau \times TR)$ and $R_{k'}(\omega_j; \tau \times TR) \leftarrow 0$ for all $\tau = 0, 1, \dots, T$.
 - 11: **end for**
 - 12: **end for**
 - 13: Apply Algorithm 1 using updated task-evoked signals $\{(Y_k(\omega_j; \tau \times TR), Y_l(\omega_j; \tau \times TR))^T\}_{\tau,j}$, newly defined reference signals $\{(R_k(\omega_j; \tau \times TR), R_l(\omega_j; \tau \times TR))^T\}_{\tau,j}$, and the repetition time TR . The estimate of ptFC $|corr(\beta_k, \beta_l)|$ is returned.
-

4 Simulations

In this section, we first describe the data generating mechanism for simulations, which mimics the trends we observed in the HCP motor-task dataset. Then, using the generated data, we illustrate the performance of the ptFCE and AMUSE-ptFCE algorithms in terms of estimating ptFC as compared to existing functional connectivity estimation approaches.

4.1 Simulation Data Generating Mechanism

We simulate 4-dimensional synthetic BOLD signals $\{(Y_k(\omega_j; \tau \times TR), Y_l(\omega_j; \tau \times TR), R_k(\omega_j; \tau \times TR), R_l(\omega_j; \tau \times TR))\}_{\tau=0}^T$, for $j = 1, 2, \dots, 308$. Each of the 4-dimensional signals contains a pair of task-evoked signals and a pair of reference signals. We apply the BOLD signal model (2.2) with the reference term model (2.4) in the stimulation process. The mechanism of simulating BOLD signals is determined by the following parameters:

(i) $TR = 0.72$ (seconds), $T = 283$; (ii) the stimulus signals in (2.2) and (2.4) applied in our simulations are those used in HCP: $N(t) = \mathbf{1}_{[86.5,98.5)}(t) + \mathbf{1}_{[162,174)}(t)$, $\tilde{N}_1(t) = \mathbf{1}_{[71.35,83.35)}(t) + \mathbf{1}_{[177.125,189.125)}(t)$, $\tilde{N}_2(t) = \mathbf{1}_{[11,23)}(t) + \mathbf{1}_{[116.63,128.63)}(t)$, $\tilde{N}_3(t) = \mathbf{1}_{[26.13,38.13)}(t) + \mathbf{1}_{[146.88,158.88)}(t)$, $\tilde{N}_4(t) = \mathbf{1}_{[56.26,68.26)}(t) + \mathbf{1}_{[131.75,143.75)}(t)$; (iii) HRF h_k and $\tilde{h}_{k,\gamma}$, for $\gamma \in \{1, 2, 3, 4\}$, are the double-gamma variate functions implemented in the R function `canonicalHRF` with default parameters; (iv) HRF h_l and $\tilde{h}_{l,\gamma}$, for $\gamma \in \{1, 2, 3, 4\}$, are the same function with parameters $\mathbf{a1}= 10$, $\mathbf{a2}= 15$, $\mathbf{b1}= 0.9$, $\mathbf{b2}= 0.9$, and $\mathbf{c}= 0.35$. We generate

$$\left\{ (\beta_k(\omega_j), \beta_l(\omega_j))^T \right\}_{j=1}^{308} \sim_{iid} MVN(\boldsymbol{\mu}_\beta, \mathbf{V}_\beta) \text{ and } \left\{ (\tilde{\beta}_{k,\gamma}(\omega_j), \tilde{\beta}_{l,\gamma}(\omega_j))^T \right\}_{j=1}^{308} \sim_{iid} MVN(\boldsymbol{\mu}^{(\gamma)}, \mathbf{V}^{(\gamma)}),$$

for $\gamma \in \{1, 2, 3, 4\}$, where the collections of random vectors $\{(\tilde{\beta}_{k,\gamma}(\omega_j), \tilde{\beta}_{l,\gamma}(\omega_j))\}_{j=1}^{308}$, for $\gamma \in \{1, 2, 3, 4\}$, are mutually independent and are independent of the collection $\{(\beta_k(\omega_j), \beta_l(\omega_j))^T\}_{j=1}^{308}$, and $\boldsymbol{\mu}_\beta = \boldsymbol{\mu}^{(\gamma)} = (0, 0)^T$,

$$\mathbf{V}^{(\gamma)} = \begin{pmatrix} 2 & 0.3 \times \sqrt{6} \\ 0.3 \times \sqrt{6} & 3 \end{pmatrix}, \text{ for } \gamma = 1, 2, 3, 4, \quad \mathbf{V}_\beta = \begin{pmatrix} 2 & \sqrt{6}\rho \\ \sqrt{6}\rho & 3 \end{pmatrix}, \text{ for } \rho = 0.25, 0.5, 0.75. \quad (4.1)$$

The values ρ in (4.1) are the true values of ptFC in this simulation study. For each $j \in \{1, 2, \dots, 308\}$ and $k' \in \{k, l\}$, the simulated random noise $\{\epsilon_{k'}(\omega_j; \tau \times TR)\}_{\tau=0}^T$ in (2.2) are iid generated from $MVN(\boldsymbol{\mu}_n, \mathbf{V}_n)$, where the random noise signals for different ω_j are independent of each other and

$$\boldsymbol{\mu}_n = \begin{pmatrix} 0 \\ 0 \end{pmatrix}, \quad \mathbf{V}_n = \begin{pmatrix} 1 & 0.2 \\ 0.2 & 1 \end{pmatrix}. \quad (4.2)$$

The BOLD signals in this simulation study are generated by the following two steps. **Step 1**, for each $j \in \{1, 2, \dots, 308\}$ and $k' \in \{k, l\}$, we generate $\{\tilde{\beta}_{k',\gamma}(\omega_j) | \gamma = 1, 2, 3, 4\}$ and $\{\epsilon_{k'}(\omega_j; \tau \times TR)\}_{\tau=0}^T$ using the mechanism presented above, while the simulated reference signal $\{R_{k'}(\omega_j; \tau \times TR)\}_{\tau=0}^T$ is defined by

$$R_{k'}(\omega_j; \tau \times TR) = 9000 + \left\{ \sum_{\gamma=1}^4 \tilde{\beta}_{k',\gamma}(\omega_j) \times (\tilde{N}_\gamma * \tilde{h}_{k,\gamma})(\tau \times TR) \right\} + \epsilon_{k'}(\omega_j; \tau \times TR). \quad (4.3)$$

Step 2, we generate another pair of realizations of $\{\tilde{\beta}_{k',\gamma}(\omega_j) | \gamma = 1, 2, 3, 4\}$ and $\{\epsilon_{k'}(\omega_j; \tau \times TR)\}_{\tau=0}^T$ and compute another realization of the reference signal $\{R_{k'}(\omega_j; \tau \times TR)\}_{\tau=0}^T$ using (4.3), then we generate

$\{(\beta_k(\omega_j), \beta_l(\omega_j))^T\}_{j=1}^{308}$ and compute the simulated task-evoked signals under the stimulus $N(t)$ as follows.

$$Y_{k'}(\omega_j; \tau \times TR) = \beta_{k'}(\omega_j) \times (N * h_{k'}) (\tau \times TR) + R_{k'}(\omega_j; \tau \times TR) \text{ for } \tau = 0, 1, \dots, T \text{ and } k' \in \{k, l\}.$$

These two simulation steps can be interpreted as follows: the experiment for each participant ω_j has two parts; in the first, participant ω_j is at rest and reference signals $R_{k'}(\omega_j; t)$ are observed; in the second part, the participant perform stimulus $N(t)$, and task-evoked signals $Y_{k'}(\omega_j; t)$ are observed. Although the signals obtained during the second part of the experiment contain reference signals, these reference signals are independent of the reference signals observed in the first part of the experiment. The upper panel of Figure 4 presents a pair of the synthetic task-evoked signals $\{Y_k(\omega_j; t), Y_l(\omega_j; t)\}_{t \in \mathcal{T}}$ for a participant ω_j . In these simulated signals, we view $N(t)$ as the task stimuli of interest and $\tilde{N}_\gamma(t)$, for $\gamma = 1, 2, 3, 4$, as stimuli not of interest, again following the set-up of the HCP motor-task study dataset analyzed in this paper.

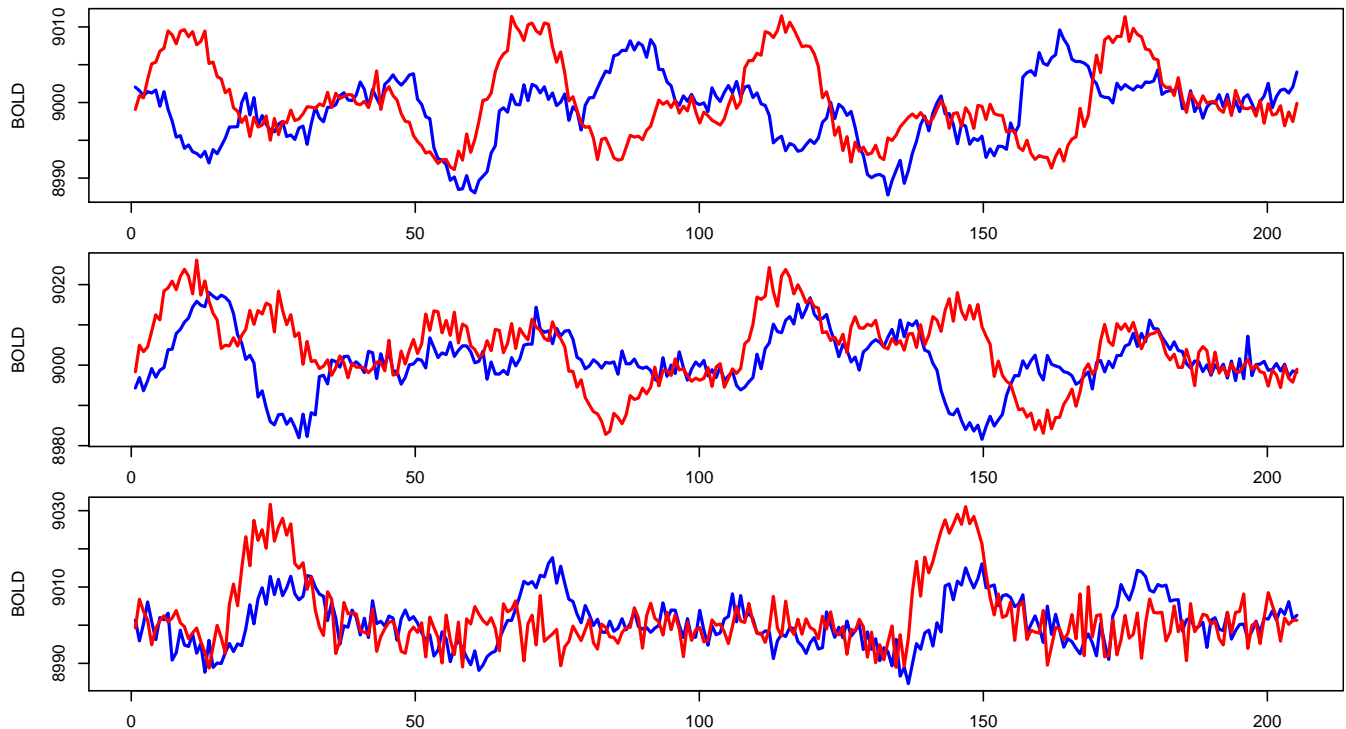


Figure 4: In all three panels, the blue and red curves represent the synthetic task-evoked signals at the k^{th} and l^{th} nodes, respectively. **Upper:** A pair of synthetic task-evoked signals simulated using the data generating mechanism in Section 4.1. **Middle:** Synthetic task-evoked signals simulated with $\lambda = 2$ in (4.4). **Lower:** Synthetic task-evoked signals simulated with $\lambda = 5$ in (4.4).

4.2 Performance of the ptFCE and AMUSE-ptFCE Algorithms

Using the simulation mechanism in Section 4.1, we simulate $\{(\beta_k(\omega_j), \beta_l(\omega_j))\}_{j=1}^{308}$ and the corresponding task-evoked and reference signals. Then we compute the sample correlation between $\{\beta_k(\omega_j)\}_{j=1}^{308}$ and $\{\beta_l(\omega_j)\}_{j=1}^{308}$ across all ω_j . The absolute value of this correlation is denoted as $\hat{\rho}_{true}$. Lastly, we apply the ptFCE algorithm (Algorithm 1) to estimate ptFC using these task-evoked and reference signals and apply the AMUSE-ptFCE algorithm (Algorithm 2) to estimate ptFC from the task-evoked signals. The estimates from Algorithms 1 and 2 are denoted by $\hat{\rho}_1$ and $\hat{\rho}_2$, respectively. Repeating the simulation procedure 100 times, we obtain 100 triplets $(\hat{\rho}_{true}, \hat{\rho}_1, \hat{\rho}_2)$. The differences $(\hat{\rho}_1 - \hat{\rho}_{true})$ and $(\hat{\rho}_2 - \hat{\rho}_{true})$ measure the accuracy of Algorithms 1 and 2. The summary of these differences is presented in Table 1.

	$\rho = 0.25$	$\rho = 0.5$	$\rho = 0.75$
mean of $\{\hat{\rho}_1 - \hat{\rho}_{true}\}$	0.07801	0.04620	0.02891
sd of $\{\hat{\rho}_1 - \hat{\rho}_{true}\}$	0.04734	0.03207	0.02775
mean of $\{\hat{\rho}_2 - \hat{\rho}_{true}\}$	-0.02745	-0.08420	-0.1461
sd of $\{\hat{\rho}_2 - \hat{\rho}_{true}\}$	0.03562	0.03559	0.02685

In all 100 simulations in Table 1, the noise $\{\epsilon_{k'}(\omega_j; \tau \times TR)\}_{\tau=0}^T$ is determined by the variance \mathbf{V}_n in (4.2). To illustrate the influence of \mathbf{V}_n on the accuracy of the ptFCE and AMUSE-ptFCE algorithms, we replace the \mathbf{V}_β and \mathbf{V}_n in (4.1, 4.2) with the following matrices.

$$\mathbf{V}_\beta = \begin{pmatrix} 2 & \sqrt{6} \times 0.5 \\ \sqrt{6} \times 0.5 & 3 \end{pmatrix}, \quad \mathbf{V}_n = \lambda \begin{pmatrix} 2 & 0.4 \\ 0.4 & 3 \end{pmatrix}, \quad \text{where } \lambda \in (0.1, 5). \quad (4.4)$$

Examples of the task-evoked signals simulated using this mechanism with $\lambda = 2$ and $\lambda = 5$ are presented in the middle and lower panels of Figure 4, respectively. For each fixed $\lambda \in (0.1, 5)$, we generate 100 simulated data sets using the mechanism in Section 4.1 and compute the corresponding 100 triplets $(\hat{\rho}_{true}, \hat{\rho}_1, \hat{\rho}_2)$. Then the mean and sd of the differences $(\hat{\rho}_j - \hat{\rho}_{true})$, for $j = 1, 2$, across all 100 simulated populations are computed. The relationship between $(\hat{\rho}_1 - \hat{\rho}_{true})$, $(\hat{\rho}_2 - \hat{\rho}_{true})$, and the noise variance scale λ in this simulation study is presented by Figure 5.

From the analyses above, we conclude that when both task-evoked and reference signals are available, the ptFCE algorithm is applicable and performs well in terms of estimating ptFC. Although it tends to slightly overestimate ptFC, the corresponding bias is small. Additionally, Figure 5 shows that, as the random noise variance increases, the bias and variance of ptFCE estimates increase as well, though moderately. When the

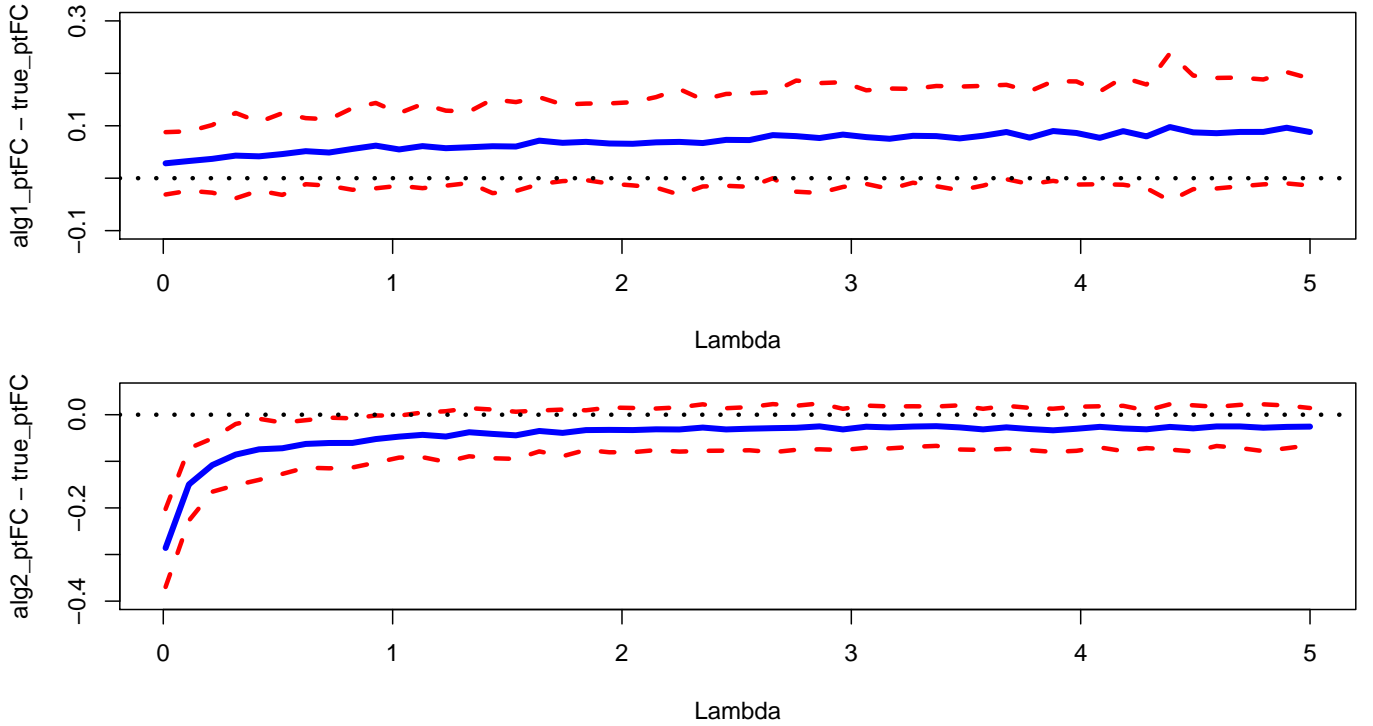


Figure 5: In each of the two panels, the blue curve presents the *mean* of 100 differences $(\hat{\rho}_j - \hat{\rho}_{true})$ with $j \in \{1, 2\}$, the red dashed curves present the 95% Wald confidence interval, i.e., $mean \pm 1.96 \times sd$, and the black dotted line indicates the zero value on the vertical axis. **Upper:** The relationship between $(\hat{\rho}_1 - \hat{\rho}_{true})$ and λ presenting the influence of random noise on the ptFCE algorithm. **Lower:** The relationship between $(\hat{\rho}_2 - \hat{\rho}_{true})$ and λ presenting the influence of random noise on the AMUSE-ptFCE algorithm.

random noise variance is large, the AMUSE-ptFCE algorithm performs well in estimating ptFC. Although it tends to underestimate ptFC, the corresponding bias is small when the random noise variance is large.

Next, we compare our proposed algorithms in terms of estimating pFC with the following existing approaches: beta-series regression, *naive Pearson correlation*, *task Pearson correlation*, and coherence analysis. We apply the simulation mechanism in Section 4.1 with \mathbf{V}_β defined by (4.1) except $\rho \in \{0, 0.25, 0.5, 0.75, 1\}$ and \mathbf{V}_n defined by (4.2). For each ρ , the ptFC estimated using the ptFCE algorithm is denoted by $\hat{\rho}_1^{ptFCE}$, while the estimated ptFC by the AMUSE-ptFCE algorithm is denoted by $\hat{\rho}_2^{ptFCE}$. In the implementation of the AMUSE-ptFCE algorithm, the input reaction delay $t_{0,k'}$ and HRF $h_{k'}$ are set to be corresponding default values in Algorithm 2. The existing methods are implemented as follows.

Beta-series regression: We apply the procedure described in Chapter 9.2 of Ashby (2019) to estimate task-evoked FC using beta-series regression, except we ignore the “nuisance term” therein. For each $\rho \in \{0, 0.25, 0.5, 0.75, 1\}$ and ω_j , we apply beta-series regression to task-evoked signals $\{Y_k(\omega_j; \tau \times TR), Y_l(\omega_j; \tau \times TR) | \tau = 0, 1, \dots, T\}$, estimate the FC evoked by $N(t)$, and denote the estimated quantity by $\hat{\rho}_j^{betaS}$. Then we compute the median of $\{\hat{\rho}_j^{betaS}\}_{j=1}^{308}$ across all j and denote it by $\hat{\rho}_M^{betaS}$.

Naive Pearson correlation: For each ρ and ω_j , we compute the Pearson correlation between $\{Y_k(\omega_j; \tau \times TR)\}_\tau$ and $\{Y_l(\omega_j; \tau \times TR)\}_\tau$ across all $\tau = 0, 1, \dots, T$ and denote the absolute value of this correlation by $\hat{\rho}_j^{naiveCorr}$. Let $\hat{\rho}_M^{naiveCorr}$ denote the median of $\{\hat{\rho}_j^{naiveCorr}\}_{j=1}^{308}$ across all j .

Task Pearson correlation: For each ρ and ω_j , we compute the Pearson correlation between $\{Y_k(\omega_j; \tau \times TR) | N(\tau \times TR) = 1\}$ and $\{Y_l(\omega_j; \tau \times TR) | N(\tau \times TR) = 1\}$ across all τ such that $N(\tau \times TR) = 1$ and denote the absolute value of this correlation by $\hat{\rho}_j^{taskCorr}$. We compute the median of $\{\hat{\rho}_j^{taskCorr}\}_{j=1}^{308}$ across all j and denote it by $\hat{\rho}_M^{taskCorr}$.

Coherence analysis: For each ρ and ω_j , we compute the coherence between task-evoked signals $\{Y_k(\omega_j; \tau \times TR)\}_\tau$ and $\{Y_l(\omega_j; \tau \times TR)\}_\tau$ by the R function `coh` in package `seewave`. The coherence is a function $coh_{\rho,j}(\xi)$ of $\xi \in (0, 1/(2 \times TR))$. Since HRF acts as a band-pass filter (typically 0 – 0.15 Hz, Aguirre et al. (1997)), we compute the median of $\{coh_{\rho,j}(\xi) | 0 < \xi < 0.15\}$ across all $\xi \in (0, 0.15)$ and denote it by $\hat{\rho}_j^{Coh}$. Finally, the median of $\{\hat{\rho}_j^{Coh}\}_{j=1}^{308}$ across all j is denoted by $\hat{\rho}_M^{Coh}$.

For each $\rho \in \{0, 0.25, 0.5, 0.75, 1\}$, we repeat the procedures above for 100 simulated data sets and obtain 100 estimated vectors $(\hat{\rho}_{true}, \hat{\rho}_1^{ptFCE}, \hat{\rho}_2^{ptFCE}, \hat{\rho}_M^{betaS}, \hat{\rho}_M^{naiveCorr}, \hat{\rho}_M^{taskCorr}, \hat{\rho}_M^{Coh})$. Instead of considering the specific values of these measurements, we are interested in grading the strength of the pairwise connectivity, e.g., the FC between two nodes is either *extremely strong*, *strong*, *median*, *weak*, or *extremely weak*. In addition, these different approaches potentially use slightly different numerical scales for measuring FC strength. Analogously, whether the Fahrenheit or Celsius scale system is used, we would conclude that Death Valley and Antarctica are the hottest and coldest places on earth, respectively, even though these two systems are using different numerical measurements. Therefore, we compare the performance of these approaches by their “graded version” instead of considering the numerical values. Specifically, the five values $\rho \in \{0, 0.25, 0.5, 0.75, 1\}$ correspond to five grades: $0 \mapsto$ grade 1 (extremely weak), $0.25 \mapsto$ grade 2 (weak), $0.5 \mapsto$ grade 3 (median), $0.75 \mapsto$ grade 4 (strong), $1 \mapsto$ grade 5 (extremely strong), i.e., $\rho \mapsto$ grade $z = order(\rho)$, where $order(\rho)$ denotes the z^{th} smallest number ρ in $\{0, 0.25, 0.5, 0.75, 1\}$; if an estimation approach results in a correct estimate of grade $order(\rho)$, we conclude that this approach is accurate, e.g., the ptFCE algorithm is accurate if $order(\hat{\rho}_1^{ptFCE}) = order(\rho)$ for all ρ . The accuracy of an approach is measured by its “correct grading rate,” i.e., the rate of $order(\hat{\rho}_1^{ptFCE}) = order(\rho)$ across all 100 simulations. A summary of the accuracy of all estimation approaches described above is presented in Table 2.

The ptFCE and AMUSE-ptFCE algorithms perform similarly well in grading ptFC, although the AMUSE-ptFCE algorithm is based on task-evoked signals only. The naive and task Pearson correlation approaches perform well in grading ptFC under the framework provided by Definition 2.1, although not as good as the

Table 2: Performance in the estimation of $order(\rho)$

	$\rho = 0$	$\rho = 0.25$	$\rho = 0.5$	$\rho = 0.75$	$\rho = 1$
Rate of $order(\hat{\rho}_1^{ptFCE}) = order(\rho)$	94%	94%	100%	100%	100%
Rate of $order(\hat{\rho}_2^{ptFCE}) = order(\rho)$	99%	99%	99%	98%	98%
Rate of $order(\hat{\rho}_M^{betaS}) = order(\rho)$	12%	18%	26%	21%	17%
Rate of $order(\hat{\rho}_M^{naiveCorr}) = order(\rho)$	86%	74%	76%	86%	92%
Rate of $order(\hat{\rho}_M^{taskCorr}) = order(\rho)$	96%	91%	92%	96%	99%
Rate of $order(\hat{\rho}_M^{Coh}) = order(\rho)$	52%	34%	32%	36%	65%

ptFCE and AMUSE-ptFCE algorithms. Under the framework of Definition 2.1, beta-series regression and coherence analysis do not provide informative grading results.

In all the simulation studies, using a PC with a 2.4 GHz 8-Core Intel Core i9 processor and 32 GB 2400 MHz DDR4 memory, all estimation approaches take less than 30 seconds to compute the corresponding estimate for each simulated data set.

5 Data Analysis

In this section, we present results obtained by the estimation of ptFC using a data set in the task-evoked functional MRI component of HCP. For comparison, we apply the AMUSE-ptFCE algorithm and existing methods to measure FC in the database of 308 participants from HCP performing motor tasks. The details of the experimental design and corresponding parameters are available on the HCP website and in Barch et al. (2013). As described in Section 1, the participants in this experiment were asked to perform five tasks: tap their left/right fingers, squeeze their left/right toes, and move their tongue. We model squeezing right toes as the task of interest with two 12-second task blocks and the corresponding task stimulus signal is $N^{rt}(t) = \mathbf{1}_{[86.5,98.5)}(t) + \mathbf{1}_{[162,174)}(t)$. The stimulus signals of the four nuisance stimuli are represented as $\tilde{N}_1(t) = \mathbf{1}_{[71.35,83.35)}(t) + \mathbf{1}_{[177.125,189.125)}(t)$, $\tilde{N}_2(t) = \mathbf{1}_{[11,23)}(t) + \mathbf{1}_{[116.63,128.63)}(t)$, $\tilde{N}_3(t) = \mathbf{1}_{[26.13,38.13)}(t) + \mathbf{1}_{[146.88,158.88)}(t)$, and $\tilde{N}_4(t) = \mathbf{1}_{[56.26,68.26)}(t) + \mathbf{1}_{[131.75,143.75)}(t)$. The onsets of all task blocks vary across participants. Nevertheless, the corresponding onsets of any two participants differ in less than 0.1 seconds. Therefore, we assume that all participants share the same stimulus signals.

Before estimating FC, we compute region-specific time courses using the AAL atlas (Tzourio-Mazoyer et al. (2002)) that consists of 120 brain regions. For each region, we extract the voxel-specific time series in that region and compute their spatial average for each time point. As a result, we obtain 120 time courses corresponding to the 120 regions of interest. We select the left precentral gyrus (PreCG.L) as the seed region since it is located in the primary motor cortex and the motions of the right toe are associated with the

left hemisphere of the brain. We measure the FC induced by $N(t)$ at a population level between the seed region and all other regions using the following five approaches: the AMUSE-ptFCE algorithm, naive and task Pearson correlation methods, beta-series regression, and coherence analysis.[†] The detailed procedures of applying these approaches are described in Section 4.2.

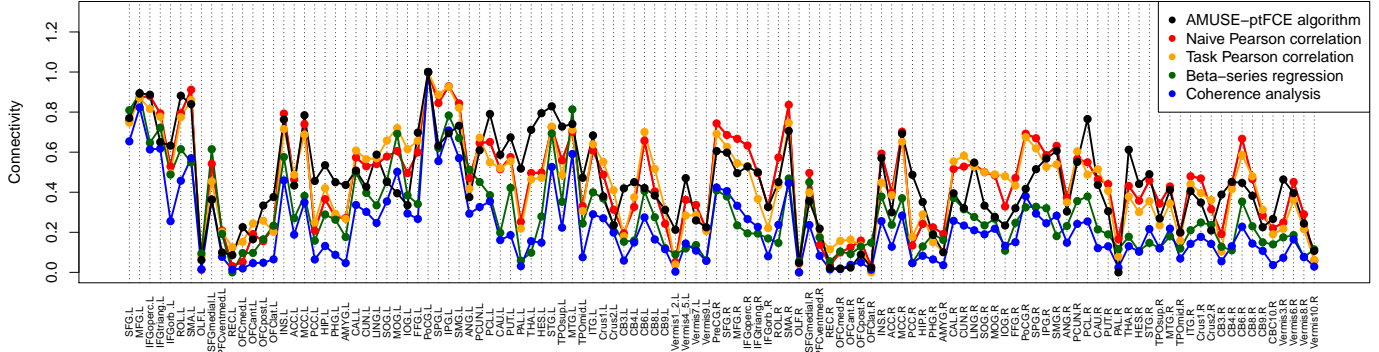


Figure 6: Illustration of estimation results from five FC estimation methods. The horizontal axis indicates the 116 regions. The abbreviations of region names are provided in the data set `aa12.120` in the R package `brainGraph`. The vertical axis presents the standardized connectivity measurements between each region and the seed region `PreCG.R`.

Suppose $\mathcal{X}_{r,j}$, for $r = 1, 2, \dots, 116$ and $j = 1, \dots, 5$, are the estimated FC between `PreCG.L` and 116 regions[†] computed using the AMUSE-ptFCE algorithm, naive Pearson correlation, task Pearson correlation, beta-series regression, and coherence analysis indexed by j . Since these estimation approaches use slightly different scales, we standardize the estimates to enable comparisons as follows $\mathcal{X}_{r,j}^{(st)} = \frac{\mathcal{X}_{r,j} - \min\{\mathcal{X}_{r',j}\}_{r'=1}^{116}}{\max\{\mathcal{X}_{r',j}\}_{r'=1}^{116} - \min\{\mathcal{X}_{r',j}\}_{r'=1}^{116}}$, for $r = 1, 2, \dots, 116$ and $j = 1, \dots, 5$. The standardized versions of the estimates are presented in Figure 6. As illustrated in Figure 6, the five methods result in similar estimated FC patterns. Specifically, the estimated FC tend to be relatively large/small simultaneously in most regions when comparing between the five methods. Therefore, all five methods provide approximately the same population-level FC structure indicating that our proposed estimation approach has similar performance to widely used Pearson correlation, beta-series regression, and coherence analysis approaches. In the meantime, our proposed AMUSE-ptFCE algorithm is based on the model proposed in Section 2 providing a clear interpretation in applications and has several advantages when compared to the competitor methods as described in Section 2.2. In addition, based on our proposed AMUSE-ptFCE algorithm estimates for FC, we identify high connectivity between several regions and the seed region that are missed by the competitor methods. Specifically, we obtain high FC between the seed region and left/right thalamus (passing motor signals to the cerebral cortex), left/right paracentral lobule (motor nerve supply to the lower extremities), left superior temporal gyrus (containing

[†] Because of numerical issues, we omit the regions `CB7.L`, `CB7.R`, and `CB10.L` and investigate the rest 117 regions.

the auditory cortex), and left Heschl gyrus (in the area of primary auditory cortex). These regions are related to the motor function or auditory cortex, and have the potential of contributing to understanding the functional connectivity between precentral gyrus and the rest of the brain regions.

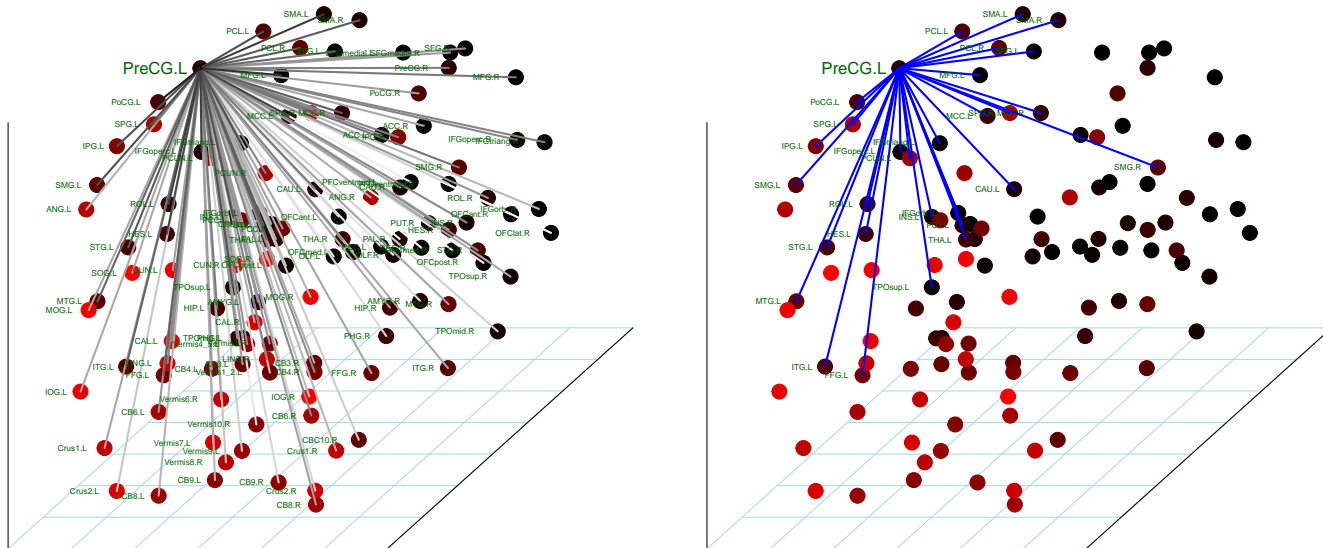


Figure 7: Each dot denotes a region from the AAL atlas, located using its corresponding MNI coordinates. The abbreviated region names are given next to each dot. We apply the AMUSE-ptFCE algorithm to estimate the ptFC between region `PreCG.L` and each of the rest 116 regions. In the left panel, we use grayscale coloring of the edges to indicate the magnitude of ptFC between the corresponding two vertices; specifically, the larger a ptFC, the darker the line segment connecting the corresponding region pair. In the right panel, the presented blue line segments indicate the first 30 largest ptFC estimated by the AMUSE-ptFCE algorithm among all 116 regions.

To further visualize the ptFC induced by the task of interest, we apply the MNI space coordinates of the 117 regions from the AAL atlas, where the three-dimensional coordinates are obtained from the data set `aal2.120` in R package `brainGraph`. The regions are depicted by their MNI coordinates in Figure 7. The grayscale shade of the edges connecting each region to the seed region illustrates the magnitude of FC between the corresponding region and the seed region (Figure 7, left panel), while the edges in the right panel of Figure 7 present the highest FC values. These plots show that most of the large estimated ptFC values are in the left brain. This is expected, since it is known that behaviors of extremities are functionally associated with contralateral brain regions (Nieuwenhuys et al., 2014).

6 Conclusions and Further Discussions

This paper proposes a model of the random effect form for task-evoked BOLD signals in fMRI studies. Based on this model, we define a rigorous measurement of the task-evoked functional connectivity at a population level. The newly defined ptFC framework has a clear interpretation in applications. We propose two algorithms, i.e., the ptFCE and AMUSE-ptFCE algorithms, for the estimation of ptFC. Simulation studies show that these two algorithms perform well in estimating ptFC. We apply the AMUSE-ptFCE algorithm to estimate FC in a motor-task dataset publicly available from the HCP. The data analysis results show that the AMUSE-ptFCE algorithm results in similar FC patterns to the widely used Pearson correlation, beta-series regression, and coherence analysis approaches. Additionally, the AMUSE-ptFCE algorithm indicates that the FC induced by squeezing right toes is mainly restricted in the left brain regions as expected.

After estimating ptFC κ , an immediate question is to decide which pairs of nodes are functionally connected. In many applications, estimated FC values are compared to a pre-defined cut-off to identify functionally connected nodes. This question can be presented by the hypothesis test $H_0 : \kappa \geq \kappa^*$ vs. $H_1 : \kappa < \kappa^*$, where κ^* is a predetermined threshold. If H_0 is rejected, the corresponding pair of nodes are not functionally connected; otherwise, they are functionally connected. We plan to develop a rigorous and computationally efficient approach for performing this hypothesis test. If a threshold κ^* is given, a bootstrap approach can be implemented to perform the hypothesis test. In most applications, the determination of a threshold κ^* for ptFC can be ambiguous. Cross-validation methods may be considered for determining the threshold. Instead of choosing a single threshold κ^* and applying hypothesis testing, an alternative approach for describing the FC structure using the estimated ptFC is to test all possible thresholds $\kappa^* \in (0, 1)$. Lee et al. (2011) propose using the theory of *persistent homology* for modeling all thresholds. Future research may consider combination of persistent homology theory and the proposed ptFC.

7 Acknowledgements

The project herein was supported by Grant Number 5P20GM103645 from the National Institute of General Medical Sciences.

8 Appendix

Lemma 8.1. *If $f : \mathcal{T} \rightarrow \mathbb{R}$ is not constant zero, its Fourier transform $\widehat{f}(\xi)$ has at most finitely many zero points - $\xi \in \mathbb{R}$ such that $\widehat{f}(\xi) = 0$ - in any compact subset of \mathbb{R} .*

Proof. Define the complex function $\Phi_f(z) := \frac{1}{T+1} \sum_{\tau=0}^T f(\tau \times TR) e^{-2\pi z(\tau \times TR)}$, for all $z = \eta + i\xi \in \mathbb{C}$. Since it is straightforward that $\Phi_f(z)$ satisfies the *Cauchy-Riemann* equation $\frac{\partial}{\partial \bar{z}} \Phi_f(z) = 0$, where $\frac{\partial}{\partial \bar{z}} = \frac{1}{2}(\frac{\partial}{\partial \eta} + i \frac{\partial}{\partial \xi})$ is a Wirtinger derivative, the Looman–Menchoff theorem implies that $\Phi_f(z)$ is a holomorphic function. Then the zero points of $\Phi_f(z)$ are isolated, i.e., every zero point has a neighbourhood that does not contain any other zero point. Therefore, $\widehat{f}(\xi) = \Phi_f(i\xi)$ implies the desired result. \square

Theorem 8.1. *Suppose signals $\{Y_k(\omega; t) | t \in \mathcal{T}\}_{k=1}^K$, for $\omega \in \Omega$, are defined as in (2.2), $\mathbb{E}\beta_k = \mathbb{E}R_k(t) = 0$, and $t_{0,k} = \tau_{0,k} \times TR$ with some $\tau_{0,k} \in \mathbb{Z}$ for all $k = 1, 2, \dots, K$ and $t \in \mathcal{T}$. Let the random variable $U : \Omega \rightarrow \mathcal{T}$ be uniformly distributed on \mathcal{T} . Furthermore, we assume that $U(\omega)$, $\{\beta_k(\omega)\}_{k=1}^K$, and $\{R_k(\omega; t) | t \in \mathcal{T}\}_{k=1}^K$ are independent. Then, the autocovariance differences in (3.5) depend only on s , the Fourier transforms of $\mathcal{A}(s)$ defined in (3.5) are $\widehat{\mathcal{A}}_{kl}(\xi) = \mathbb{E}(\beta_k \beta_l) \times |\widehat{N}(\xi)|^2 \overline{\widehat{h}_k(\xi)} \widehat{h}_l(\xi) e^{2\pi i(t_{0,k} - t_{0,l})\xi}$, and $\mathcal{C}_{kl}(\xi) = |\text{corr}(\beta_k, \beta_l)|$ for all $\xi \in \mathbb{R}$, where $\mathcal{C}_{kl}(\xi)$ is defined in (3.6).*

Proof. The independence between $U(\omega)$, $\{\beta_k(\omega)\}_{k=1}^K$, and $\{R_k(\omega; t) | t \in \mathcal{T}\}_{k=1}^K$ implies

$$\begin{aligned}
& \mathbb{E}[Y_k(t - U)Y_l(t + s - U)] - \mathbb{E}[R_k(t - U)R_l(t + s - U)] \\
&= \mathbb{E}(\beta_k \beta_l) \times \mathbb{E}[(N * h_k)(t - t_{0,k} - U) \times (N * h_l)(t + s - t_{0,l} - U)] \\
&= \mathbb{E}(\beta_k \beta_l) \times \frac{1}{T+1} \sum_{u=0}^T \left\{ (N * h_k)((\tau - \tau_{0,k} - u) \times TR) \times (N * h_l)((\underline{s} + \tau_{0,k} - \tau_{0,l}) \times TR + (\tau - \tau_{0,k} - u) \times TR) \right\} \\
&= \mathbb{E}(\beta_k \beta_l) \times \frac{1}{T+1} \sum_{v=-(\tau - \tau_{0,k})}^{T - (\tau - \tau_{0,k})} \left\{ (N * h_k)(-v \times TR) \times (N * h_l)((\underline{s} + \tau_{0,k} - \tau_{0,l}) \times TR - v \times TR) \right\} \\
&= \mathbb{E}(\beta_k \beta_l) \times [N * h_k(\cdot)] * [N * h_l](s + (t_{0,k} - t_{0,l})), \tag{8.1}
\end{aligned}$$

which only depends on s and does not depend on t , where the last equality follows from the periodic extension (3.1) and the definition of convolution. Then, we have the following Fourier transform

$$\widehat{\mathcal{A}}_{kl}(\xi) = \mathbb{E}(\beta_k \beta_l) \times \overline{\widehat{(N * h_k)}(\xi)} \widehat{(N * h_l)}(\xi) e^{2\pi i(t_{0,k} - t_{0,l})\xi} = \mathbb{E}(\beta_k \beta_l) \times \left| \widehat{N}(\xi) \right|^2 \overline{\widehat{h}_k(\xi)} \widehat{h}_l(\xi) e^{2\pi i(t_{0,k} - t_{0,l})\xi},$$

for all $\xi \in \mathbb{R}$ implying $\mathcal{C}_{kl}(\xi) = |\text{corr}(\beta_k, \beta_l)|$ for all $\xi \in \mathbb{R}$. \square

Lemma 8.2. *The vector-valued stochastic process $\mathbf{Z}(\omega) = \{(Z_1(\omega; t), Z_2(\omega; t), \dots, Z_K(\omega; t))^T\}_{t \in \mathcal{T}}$ is defined on (Ω, \mathbb{P}) and weakly stationary with mean zero, $U : \Omega \rightarrow \mathcal{T}$ is a uniformly distributed, and $U(\omega)$ and $\mathbf{Z}(\omega)$ are independent. Then the vector-valued stochastic process $\{(Z_1(\omega; t - U(\omega)), Z_2(\omega; t - U(\omega)), \dots, Z_K(\omega; t - U(\omega)))^T\}_{t \in \mathcal{T}}$ is weakly stationary with mean zero as well. Additionally, $\mathbb{E}[Z_k(t - U)Z_l(t + s - U)] = \mathbb{E}[Z_k(0)Z_l(s)]$, for all $k, l = 1, 2, \dots, K$.*

Proof. Let $P_{\mathbf{Z}} = P_{\mathbf{Z}}(dz)$ be the probability measure on the path space $(\mathbb{R}^{\mathcal{T}})^K$ associated with the K -vector-valued stochastic process \mathbf{Z} , i.e., $P_{\mathbf{Z}} = \mathbb{P} \circ \mathbf{Z}^{-1}$. The probability measure on \mathcal{T} associated with U is denoted as μ , i.e., $\mu = \mathbb{P} \circ U^{-1}$. Since \mathbf{Z} and U are independent, the probability measure on $(\mathbb{R}^{\mathcal{T}})^K \times \mathcal{T}$ associated with the joint distribution (\mathbf{Z}, U) is the product measure $P_{\mathbf{Z}} \otimes \mu$, i.e., $P_{\mathbf{Z}} \otimes \mu = \mathbb{P} \circ (\mathbf{Z}, U)^{-1}$. Then the zero mean of $Z_k(t)$ implies $\mathbb{E}Z_k(t - U) = \int_{\mathcal{T}} \mathbb{E}[Z_k(t - U)|U = u]\mu(du) = \int_{\mathcal{T}} \mathbb{E}Z_k(t - u)\mu(du) = 0$. Let $s \in \mathcal{T}$ and $k, l \in \{1, 2, \dots, K\}$ be fixed, for each $t^* \in \mathcal{T}$, we define the following map.

$$\Phi_{t^*} : (\mathbb{R}^{\mathcal{T}})^K \rightarrow \mathbb{R}, \quad \{(z_1(t), z_2(t), \dots, z_K(t))\}_{t \in \mathcal{T}} \mapsto z_k(t^*)z_l(t^* + s).$$

Then Fubini's theorem implies the following representation.

$$\mathbb{E}[Z_k(t - U)Z_l(t + s - U)] = \mathbb{E}[\Phi_{t-U}(\mathbf{Z})] = \int_{(\mathbb{R}^{\mathcal{T}})^K \times \mathcal{T}} \Phi_{t-u}(z) P_{\mathbf{Z}} \otimes \mu(dz, du) = \int_{\mathcal{T}} \left[\int_{(\mathbb{R}^{\mathcal{T}})^K} \Phi_{t-u}(z) P_{\mathbf{Z}}(dz) \right] \mu(du).$$

Since \mathbf{Z} is weakly stationary, $\int_{(\mathbb{R}^{\mathcal{T}})^K} \Phi_{t-u}(z) P_{\mathbf{Z}}(dz) = \mathbb{E}[Z_k(t - u)Z_l(t + s - u)] = \mathbb{E}[Z_k(0)Z_l(s)]$, for all $u \in \mathcal{T}$. Then $\mathbb{E}[Z_k(t - U)Z_l(t + s - U)] = \mathbb{E}[Z_k(0)Z_l(s)]$, which depends only on s . \square

Theorem 8.2. *Suppose signals $Y_k(\omega; t)$ are defined in (3.7) for all $k = 1, 2, \dots, K$, the random variable $U : \Omega \rightarrow \mathcal{T}$ is uniformly distributed, and the stochastic process $\{W(\omega; t) = (W_1(\omega; t), W_2(\omega; t), \dots, W_K(\omega; t))^T\}_{t \in \mathcal{T}}$ satisfies (i) $W(\omega; t_1)$ and $W(\omega; t_2)$ are independent if $t_1 \neq t_2$, (ii) $\Sigma_{kl} = \mathbb{E}[W_k(t)W_l(t)]$ for all $t \in \mathcal{T}$, and (iii) $W(\omega; t)$ is weakly stationary with mean zero. Assuming $\{W_k(\omega; t)|t \in \mathcal{T}\}_{k=1}^K$, $U(\omega)$, $\{\beta_k(\omega)\}_{k=1}^K$, and $\{R_k(\omega; t)|t \in \mathcal{T}\}_{k=1}^K$ are independent, we have (3.8).*

Proof. That $\{W_k(\omega; t)|t \in \mathcal{T}\}_{k=1}^K$, $U(\omega)$, $\{\beta_k(\omega)\}_{k=1}^K$, and $\{R_k(\omega; t)|t \in \mathcal{T}\}_{k=1}^K$ are independent implies $\mathcal{A}_{kl}(s) = \mathbb{E}(\beta_k \beta_l) \times I + II$, where $I = \frac{1}{T+1} \sum_{u=0}^T N * h_k((\tau - \tau_{0,k} - u) \times TR) N * h_l((\tau + \underline{s} - \tau_{0,l} - u) \times TR)$ and $II = \mathbb{E}[W_k(t - U)W_l(t + s - U)]$. The calculation in (8.1) implies that the Fourier transform of I is $|\widehat{N}(\xi)|^2 \overline{\widehat{h}_k(\xi)} \widehat{h}_l(\xi) e^{2\pi i \xi(t_{0,k} - t_{0,l})}$. Lemma 8.2 implies $II = \mathbb{E}[W_k(0)W_l(s)] = \Sigma_{kl} \times \mathbf{1}_{\{0\}}(s)$, where $\mathbf{1}_{\{0\}}(s)$ is the indicator function for the singleton $\{0\}$, and the Fourier transform of II is the constant $\Sigma_{kl}/(T + 1)$. Then $\widehat{\mathcal{A}}_{kl}(\xi) = \mathbb{E}(\beta_k \beta_l) \left| \widehat{N}(\xi) \right|^2 \overline{\widehat{h}_k(\xi)} \widehat{h}_l(\xi) e^{2\pi i \xi(t_{0,k} - t_{0,l})} + \frac{\Sigma_{kl}}{T+1}$, and (3.8) follows. \square

Proof of Theorem 3.1: Lemma 8.2 implies that, for each fixed $k \in \{1, 2, \dots, K\}$, the scalar-valued stochastic process $\{R_k(\omega; t - U(\omega))\}_{t \in \mathcal{T}}$ is weakly stationary with mean zero. The independence between $\beta_k(\omega)$ and $\{U(\omega), R_k(\omega; t) | t \in \mathcal{T}\}$ implies that $\{R_k(\omega; t - U(\omega))\}_{t \in \mathcal{T}}$ is weakly stationary with mean zero conditioning on β_k . Additionally,

$$\mathbb{E}\{J_k(t)R_k(t + s - U)|\beta_k\}(\omega) = \beta_k(\omega)\mathbb{E}\{[(N * h_k)(t - t_{0,k} - U) - C_k]\mathbb{E}[R_k(t + s - U)|U]\} \text{ a.s..}$$

Since $\mathbb{E}R_k(t) = 0$ for all $t \in \mathcal{T}$ and $U(\omega)$ is independent of $\{R_k(\omega; t)\}_{t \in \mathcal{T}}$, we have $\mathbb{E}[R_k(t + s - U)|U = u] = \mathbb{E}[R_k(t + s - u)] = 0$, for all $u \in \mathcal{T}$. Then $\mathbb{E}\{J_k(t)R_k(t + s - U)|\beta_k\} = 0$, for all s and t , and the desired result follows from Theorem 2 of Tong et al. (1991). \square

Proof of Theorem 3.2: Since \mathbf{P} is a permutation matrix and \mathbf{A} is a diagonal matrix, the equation (3.10) implies $\beta_k(\omega) = a_{1i'}/a_{2i'}$ for some $i' \in \{1, 2\}$ and $a_{2j} = 0$ when $j \neq i'$. Then (3.9) implies $a_{2i'}s_{i'}(\omega; t) = (N * h_k)(t - t_{0,k} - U(\omega)) - C_k$. Therefore, $a_{1i'}s_{i'}(\omega; t) = \frac{a_{1i'}}{a_{2i'}} \times a_{2i'}s_{i'}(\omega; t) = J_k(\omega; t)$. \square

References

- G. K. Aguirre, E. Zarahn, and M. D'Esposito. Empirical analyses of bold fmri statistics. *NeuroImage*, 5(3): 199–212, 1997.
- F. G. Ashby. *Statistical analysis of fMRI data*. MIT press, 2019.
- D. M. Barch, G. C. Burgess, M. P. Harms, S. E. Petersen, B. L. Schlaggar, M. Corbetta, M. F. Glasser, S. Curtiss, S. Dixit, C. Feldt, et al. Function in the human connectome: task-fmri and individual differences in behavior. *Neuroimage*, 80:169–189, 2013.
- P. Bloomfield. *Fourier analysis of time series: an introduction*. John Wiley & Sons, 2004.
- R. L. Buckner, W. Koutstaal, D. L. Schacter, A. M. Dale, M. Rotte, and B. R. Rosen. Functional–anatomic study of episodic retrieval: Ii. selective averaging of event-related fmri trials to test the retrieval success hypothesis. *Neuroimage*, 7(3):163–175, 1998.
- R. L. Buckner, F. M. Krienen, A. Castellanos, J. C. Diaz, and B. T. Yeo. The organization of the human cerebellum estimated by intrinsic functional connectivity. *Journal of neurophysiology*, 106(5):2322–2345, 2011.
- R. Durrett. *Probability: theory and examples*, volume 49. Cambridge university press, 2019.

- K. Friston, C. Frith, P. Liddle, and R. Frackowiak. Functional connectivity: the principal-component analysis of large (pet) data sets. *Journal of Cerebral Blood Flow & Metabolism*, 13(1):5–14, 1993.
- K. J. Friston. Functional and effective connectivity in neuroimaging: a synthesis. *Human brain mapping*, 2(1-2):56–78, 1994.
- K. J. Friston. Functional and effective connectivity: a review. *Brain connectivity*, 1(1):13–36, 2011.
- K. J. Friston, P. Jezzard, and R. Turner. Analysis of functional mri time-series. *Human brain mapping*, 1(2):153–171, 1994.
- M. Hampson, B. S. Peterson, P. Skudlarski, J. C. Gatenby, and J. C. Gore. Detection of functional connectivity using temporal correlations in mr images. *Human brain mapping*, 15(4):247–262, 2002.
- L. Hörmander. Estimates for translation invariant operators in p spaces. *Acta Mathematica*, 104(1-2):93–140, 1960.
- S. E. Joel, B. S. Caffo, P. C. van Zijl, and J. J. Pekar. On the relationship between seed-based and ica-based measures of functional connectivity. *Magnetic Resonance in Medicine*, 66(3):644–657, 2011.
- H. Lee, M. K. Chung, H. Kang, B.-N. Kim, and D. S. Lee. Discriminative persistent homology of brain networks. In *2011 IEEE international symposium on biomedical imaging: from nano to macro*, pages 841–844. IEEE, 2011.
- S.-P. Lee, T. Q. Duong, G. Yang, C. Iadecola, and S.-G. Kim. Relative changes of cerebral arterial and venous blood volumes during increased cerebral blood flow: implications for bold fmri. *Magnetic Resonance in Medicine: An Official Journal of the International Society for Magnetic Resonance in Medicine*, 45(5):791–800, 2001.
- M. A. Lindquist et al. The statistical analysis of fmri data. *Statistical science*, 23(4):439–464, 2008.
- M. J. Lowe, M. Dzemidzic, J. T. Lurito, V. P. Mathews, and M. D. Phillips. Correlations in low-frequency bold fluctuations reflect cortico-cortical connections. *Neuroimage*, 12(5):582–587, 2000.
- F. M. Miezin, L. Maccotta, J. Ollinger, S. Petersen, and R. Buckner. Characterizing the hemodynamic response: effects of presentation rate, sampling procedure, and the possibility of ordering brain activity based on relative timing. *Neuroimage*, 11(6):735–759, 2000.

- K. Müller, G. Lohmann, V. Bosch, and D. Y. Von Cramon. On multivariate spectral analysis of fmri time series. *NeuroImage*, 14(2):347–356, 2001.
- R. Nieuwenhuys, J. Hans, and C. Nicholson. *The central nervous system of vertebrates*. Springer, 2014.
- J. Rissman, A. Gazzaley, and M. D’Esposito. Measuring functional connectivity during distinct stages of a cognitive task. *Neuroimage*, 23(2):752–763, 2004.
- B. R. Rosen, R. L. Buckner, and A. M. Dale. Event-related functional mri: past, present, and future. *Proceedings of the National Academy of Sciences*, 95(3):773–780, 1998.
- Z. S. Saad, K. M. Ropella, R. W. Cox, and E. A. DeYoe. Analysis and use of fmri response delays. *Human brain mapping*, 13(2):74–93, 2001.
- D. L. Schacter, R. L. Buckner, W. Koutstaal, A. M. Dale, and B. R. Rosen. Late onset of anterior prefrontal activity during true and false recognition: an event-related fmri study. *Neuroimage*, 6(4):259–269, 1997.
- F. T. Sun, L. M. Miller, and M. D’Esposito. Measuring interregional functional connectivity using coherence and partial coherence analyses of fmri data. *Neuroimage*, 21(2):647–658, 2004.
- L. Tong, R.-W. Liu, V. C. Soon, and Y.-F. Huang. Indeterminacy and identifiability of blind identification. *IEEE Transactions on circuits and systems*, 38(5):499–509, 1991.
- N. Tzourio-Mazoyer, B. Landeau, D. Papathanassiou, F. Crivello, O. Etard, N. Delcroix, B. Mazoyer, and M. Joliot. Automated anatomical labeling of activations in spm using a macroscopic anatomical parcellation of the mni mri single-subject brain. *Neuroimage*, 15(1):273–289, 2002.
- R. Warnick, M. Guindani, E. Erhardt, E. Allen, V. Calhoun, and M. Vannucci. A bayesian approach for estimating dynamic functional network connectivity in fmri data. *Journal of the American Statistical Association*, 113(521):134–151, 2018.
- B. T. Yeo, F. M. Krienen, J. Sepulcre, M. R. Sabuncu, D. Lashkari, M. Hollinshead, J. L. Roffman, J. W. Smoller, L. Zöllei, J. R. Polimeni, et al. The organization of the human cerebral cortex estimated by intrinsic functional connectivity. *Journal of neurophysiology*, 2011.